Suspended graphene device fabrication

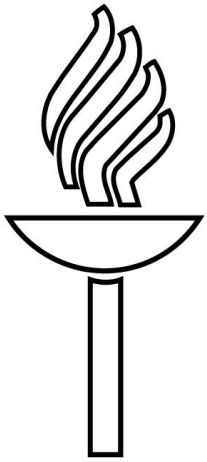

Vesa-Matti Hiltunen

Master's thesis
University of Jyväskylä
Department of Physics
March 3, 2016
Instructor: Andreas Johansson

Acknowledgments

It has been a long road, but finally I am at the end of my studies. As I am writing this, after finishing the rest of the thesis, I can't help but to think that this is the culmination point of about 20 years of education, and so I feel like taking the liberty to write a bit lengthier acknowledgments section than you normally have in a Master's thesis. Along the way there has been so many people that have helped me that there is no point in naming them all in here. Therefore, I would like to broadly thank all the great teachers that have taught me during the years prior to my studies in the University of Jyväskylä, especially all the mathematics, physics and chemistry teachers in my former high school. They helped me to get interested in sciences and gave me early on the necessary help to reach this far.

As for the more recent years, the biggest thanks goes to Andreas Johansson, who was the instructor of both my Bachelor's and Master's theses. First for offering me this project, that was challenging but not at all impossible to succeed and that also had a very clear goal, an important feature in a thesis in my opinion. Secondly, for his optimism and positive attitude, even after series of failures, and of course for good advice and guidance to overcome those setbacks. Another important person that has helped me during the project is Kevin Roberts, who has offered plenty of good advice, ideas and observations and importantly has not hesitated to be critical when needed. Other people that I would like to thank in name are Juha Koivistoinen for his help in Raman measurements, Jyrki Manninen, who also is working in graphene related project and has offered good ideas, and our laboratory engineers at the Nanoscience Center Kimmo Kinnunen and Tarmo Suppula, who keep the machines running and therefore the wheels of science rolling. Also, I want to thank all the people at the Nanoscience Center that have helped me, but are not named here. Finally, of course, I would like to thank my family and friends, who have helped me or put up with me throughout these years outside of the academic circles. As I said, it has been a long road, but as I look back and look ahead I know that this just the beginning of my career, and I know that I am going to fine if I have as great people supporting me as I have had thus far. So my sincerest thanks to all people mentioned above and also for anyone who finds the time to read this thesis. I hope that you find it interesting.

Jyväskylä March, 2016

Vesa-Matti Hiltunen

Abstract

In this Master's thesis the production of suspended graphene devices was studied. Graphene was synthesized using atmospheric pressure chemical vapor deposition onto copper thin films that were fabricated using electron beam evaporation. During the project, the synthesis process was improved by optimizing synthesis parameters. After synthesis graphene samples were transferred onto silicon nitride membranes, which had openings fabricated to them. The last step of the transfer was removal of PMMA support layer from graphene, which was studied using two different methods. First of these was thermal annealing and the second critical point drying after dissolving the PMMA with acetone. Samples were imaged using scanning electron microscopy, transmission electron microscopy and optical microscopy. Further characterization was done with Raman spectroscopy. As for results, after some struggle with synthesis, suspended graphene was successfully fabricated. As for different PMMA cleaning methods, thermal annealing worked with multilayer graphene, but caused single layer graphene to break. Critical point drying worked in both cases, but left residues, so best method ended up being PMMA removal by critical point drying followed by cleaning of graphene by annealing.

Tiivistelmä

Tämän pro gradu -tutkielman aiheena oli tutkia itsekantavien grafeeninäytteiden valmistusta. Grafeeni syntetisoitiin kaasufaasikasvatuksella ilmakehän paineessa kupariohutkalvoille. Kupariohutkalvot valmistattiin käyttämällä elektronisuihkuhöyrystystä. Projektin aikana synteesiprosessia parannettiin optimoimalla synteesiparametreja. Syntetisoinnin jälkeen grafeeninäytteet siirrettiin piinitridikalvoille, joihin oli valmistettu reikiä. Viimeinen vaihe siirrossa on PMMA tukikerroksen poisto grafeenin päältä, jota tutkittiin käyttämällä kahta eri menetelmää. Näistä ensimmäinen menetelmä oli lämpökäsittely ja toinen kriittisen pisteen kuivaus PMMA:n asetoniin liuottamisen jälkeen. Näytteet kuvannettiin käyttämällä pyyhkäisyelektronimikroskopiaa, läpäisyelektronimikroskopiaa sekä optista mikroskopiaa. Lisäksi näytteet karakterisoitiin käyttämällä Raman spektroskopiaa. Työn tuloksena alun synteesiongelmien jälkeen itsekantavaa grafeenia valmistettiin onnistuneesti. Eri PMMA:n poistomenetelmistä lämpökäsittely toimi monikerroksiselle grafeenille, mutta yksikerroksinen grafeeni ei selvinnyt käsittelystä. Kriittisen pisteen kuivaus toimi molemmissa tapauksissa, mutta jätti epäpuhtauksia, joten parhaaksi menetelmäksi selvisi PMMA:n poisto käyttämällä kriittisen pisteen kuivausta ja näytteiden puhdistus tämän jälkeen käyttämällä lämpökäsittelyä.

Contents

A list of abbreviations used in this thesis

OM = Optical Microscopy
SEM = Scanning Electron Microscopy
TEM = Transmission Electron Microscopy
CVD = Chemical Vapor Deposition
CPD = Critical Point Drying
RIE = Reactive Ion Etching
PMMA = Poly(methyl methacrylate)
DI water = Deionized water
IPA = Isopropanol alcohol

1 Introduction

Graphene is a two dimensional carbon allotrope, that was first time isolated in 2004 [1] by Geim and Novoselov and has since become a very popular research subject. It was brought up first as a purely theoretical concept by Wallace in 1947 to explain band theory of graphite [2], and for a long time it was only theoretical material since two dimensional crystals were believed to be unstable according to the Mermin-Wagner theorem [3]. However, graphene was still discovered and in the wake of it numerous other 2D materials were found [4].

Graphene has attracted plenty of attention due to its excellent properties. Besides of being a two dimensional material its properties also include high thermal conductivity [5], high charge carrier mobility [1], excellent mechanical strength [6], optical transparency [7] and it is also very light and flexible material.

Needless to say, because of its excellent properties, graphene has been proposed to be used in very wide variety of applications. For example it could be used in solar cells as transparent electrodes [8], as electrodes in supercapacitors [9] and in fuel cells [10]. It is also possible to use graphene in different types of sensors, such as biosensors [11], pressure sensors [12] and sensors for detecting various different gas species, for example carbon dioxide [13], nitrogen dioxide [14] and hydrogen [15]. In addition to these there are also many different electronic and optoelectronic applications like field effect transistors [16], terahertz devices [17, 18] and plasmonic devices [19].

One of the most important aspects in experimental graphene research is production of it. There are numerous ways to produce graphene and all of the methods have their own advantages and disadvantages. The first method to produce graphene was to mechanically exfoliate pyrolytic graphite using scotch tape [1], which produces randomly quite small domains of single layer graphene amongst double- and multilayer domains, which one must find and characterize before further processing. The graphene produced this way is however pure and with little defects and leads to better electrical devices [20]. This is a very time consuming and unscalable method, which is the reason why many other methods have been developed. Other graphene production methods include high temperature annealing of silicon carbide [21], reduction of graphene oxide [22] and unzipping carbon nanotubes [23]. These have their own limitations either in quality, graphene crystal sizes or cost and have suitable uses for some applications, but when talking about large area single layer graphene the most common production method is chemical vapor deposition (CVD). This is also the method used in this thesis for graphene synthesis.

Usually graphene is studied after it is transferred onto some substrate, commonly silicon with silicon dioxide thin film on it. For some applications or characterization methods, such as transmission electron microscopy, graphene should be suspended, stretched over a hole or opening. Also some of the properties of graphene can not be utilized the best way if it is on a substrate. For example charge carrier mobility in graphene is theoretically about 200000 $\mathrm{cm^2V^{-1}s^{-1}}$ [24], and mobilities close to this have been measured from suspended graphene [25] but when it is on SiO_2 the substrate causes more scattering and mobility drops roughly one order of magnitude [24].

The goal in this work was to produce suspended graphene samples. These type of samples has never been made at University of Jyväskylä. The work included im-

proving the synthesis method and testing of different transfer and cleaning methods, as well as fabrication of TEM compatible substrates. Samples were characterized using scanning electron microscopy, transmission electron microscopy and Raman spectroscopy.

2 Theoretical background

2.1 Graphene

The structure of graphene is a one atom layer thick sheet of sp^2 hybridized carbon in a honeycomb lattice and it is the thinnest known material [1]. The crystalline structure of grahpene with its unit cell is presented in Figure 1a. Graphene has two carbon atoms (A and B) per unit cell, and atoms are bound to their three nearest neighbors by σ bonds, with 120° between the bonds. These bonds are the reason for the good mechanical and thermal properties of graphene. The remaining valence electrons form π bonds, and these delocalized π electrons are responsible of the electronic transport properties of graphene.

For a long time it was thought that 2D crystals could not exist and after graphene was found it was argued that graphene is stable because it is part of a larger 3D structure, supported by substrate or part of 3D matrix. However, even suspended graphene is found to be stable because of nanoscale corrugations [26].

The two dimensional band structure of graphene is presented in Figure 1b. Valence and conduction bands touch at six points, which are called Dirac points. Because graphene has only carbon in its lattice, there is inversion symmetry, which allows one to reduce these to two points K and K'. A close-up image of low energy scale of one Dirac point is presented in Figure 1c, where can be seen that graphene has zero band gap and a linear dispersion relation given by equation $E = \pm\hbar\nu\,|\mathbf{k}|$ [27, 28], where E is the energy, c the speed of light, $\hbar$ the reduced Planck constant and $\mathbf{k}$ the wavevector. This means that at these low energy electronic states charge carriers are described by the Dirac equation for massless fermions. Since the charge carriers act as massless Dirac fermions, graphene exhibits interesting electronic phenomena, for example quantum Hall effect [29].

As a material with plenty of excellent properties, graphene has been suggested to be used in many applications instead of traditional semiconductors. Usability of graphene has however been reduced because of lack of bandgap. For this reason there has been lots of research in modification of its electronic properties by opening and tuning the band gap. Band gap opening can be done in many ways, for example by shaping graphene into a nanoribbon [30], by doping [31] or by photo oxidation [32].

Other properties besides electrical properties in graphene include high strength, thermal conduction and transparency. Graphene has been measured to be the strongest material known with a tensile strength of 130 GPa and a breaking strength 200 times higher than for steel [33, 34], which is due to its strong σ bonds. These bonds are also responsible of graphene's high thermal conduction. The graphene sheet has also been found to be impermeable to most gases even, except to helium [35]. Graphene absorbs 2.3 % of the light, and it adds up as multiples of that for the few first layers, which makes it possible to differentiate the number of layers optically when it is on a substrate or suspended.

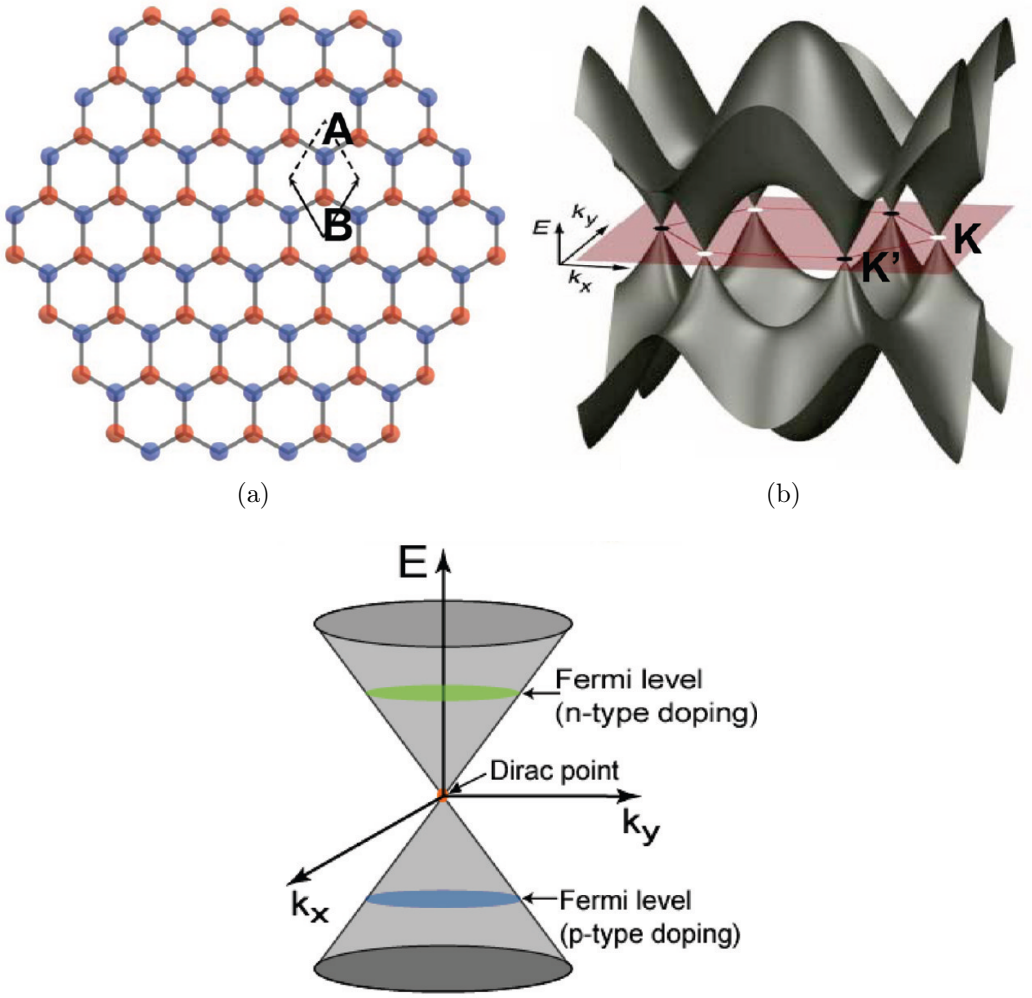

Figure 1: Crystalline and band structure of graphene. (a) Graphene crystal structure with unit cell highlighted. (b) Graphene band structure, (c) One of the Dirac points zoomed in with illustration how doping affects the Fermi level. [28]

2.2 Fabrication methods

2.2.1 Metallization by evaporation

Thin film fabrication by evaporation is a simple and widely used method. A crucible containing the wanted thin film material (target) is heated under vacuum until it evaporates. Evaporated particles travel through vacuum and hit the sample surface and solidify there because of its lower temperature, forming a thin film. Vacuum is important in order to prevent evaporated particles from colliding with gas molecules and avoid trapping of the gas into the film. It also lowers the needed temperature. Heating can be done either by using resistive heating or directing an electron beam to the material.

Resistive heating is the simplest way to heat the target material. In this method, a crucible containing the material is heated by electric current. This works with

metals that are easy to evaporate, such as aluminum or gold. A problem in this method is that there is a possibility that the crucible reacts with the target material. A more sophisticated heating method is to use electron beam heating. In this method the target is in a water cooled crucible and a focused electron beam is generated and directed to the target, using magnetic field. This causes heating to be very local and therefore it is less likely that contaminants are evaporated or that the target material reacts with the crucible. Electron beam evaporation is suitable for materials that are hard to evaporate, because of very local heating.

There are only a few parameters that can be tuned in evaporation deposition. To achieve evaporation, vapor pressure of the material must be higher than the pressure in the chamber. The pressure also has to be low enough to increase the mean free path so that the atoms or molecules arrive to the substrate without collisions. Lack of collisions prevent any chemical reactions and makes sure that evaporated atoms or molecules arrive to substrate. For these reasons the aim is to have as low pressure as possible.

Perhaps the most important parameter in evaporation is evaporation rate, which is connected to the temperature of the target material. Usually a good rate is a few nanometers per second, but it can vary with different materials. Too high rates can cause pinholes in the film, which causes tensile stress.

Evaporation is not suitable for some materials. For example alloys are usually not easy to evaporate because different elements have different vapor pressures, which changes ratios of these materials in the evaporated films. Also, stoichiometric compounds might lose the ratios when evaporated because of different vapor pressures and therefore different evaporation rates.

Thin films that are fabricated using evaporation are often amorphous. This is because of the low temperature of the substrate. When evaporated material hits a cold substrate surface it solidifies at the point where it lands without moving. Because the particles do not have the energy to arrange themselves, the film does not acquire much order, making it amorphous. If the substrate is heated, particles have more energy when they hit the surface, allowing them to diffuse and form more ordered structure. However, even with the substrate heating, the film in most cases is only polycrystalline. Crystallinity can be increased by annealing the material at high temperature.

Another notable characteristic feature of evaporation is that it is a line-of-sight method. This means that the film grows only to places that are "visible" from the target. This is caused by the fact that when material is evaporated, it travels ballistically through the vacuum without collisions. This means that for example any piece of dirt can shadow the sample, preventing the deposition, but it also enables to stop deposition quickly with only a simple mechanical substrate that can be moved between target and shutter to stop the particle flow.

Deposition thickness can be monitored by using a Quartz Crystal Microbalance (QCM). The working principle of QCM is based on single crystal quartz, which has a very precise mechanical vibration resonance frequency, which can be measured via piezoelectric effect. As material is deposited on the crystal, the mass of the system increases, which changes the resonant frequency. QCM is so precise that it allows to monitor even one or a few atomic layer changes.

2.2.2 Chemical vapor deposition

Chemical Vapor Deposition is a technique where gaseous precursors react either in gas phase or on surface, forming a solid product [36]. Usually this happens at high temperatures, but it is also possible to bring the necessary energy as light or electric discharge, which makes the CVD laser assisted or plasma assisted respectively. By far the most used method in graphene synthesis is thermal CVD, which will also be focused on here.

One of the most important aspects in graphene synthesis with CVD is the catalyst material. Many transition metals, mainly Ru, Ir, Pd, Pt, Ni and Cu, have been found to be working catalysts. There are however lots of differences between these. Most common catalysts are nickel and copper, partly because of their lower prize compared to other suitable transition metals. In general copper is a catalyst which produces single graphene layer and others bi- and multilayer graphene [37]. This has been attributed to different carbon solubilities [38]. Copper has very low carbon solubility of 0.001-0.008 wt.-% at 1084 °C and nickel significantly higher 0.6 wt.-% at 1326 °C [37]. As the graphene grows on copper the catalyst surface is covered, which deactivates it and thus, ideally, only one graphene layer is synthesized. In the case of nickel, carbon saturates in the metal during growth and once the synthesis is finished and sample is cooled, the carbon precipitates back to the surface, forming multilayer graphene. The self limiting property is so far unique to copper, making it the best choice for growing single-layer graphene. Another possibility would be to use alloys. A few studies have been made with CuNi alloy catalysts and their results seem to indicate that it is possible to control the number of graphene layers by changing Ni content in the alloy [39]. Another way could be to use NiAu alloy, in which gold is used to decrease graphene nucleation [40]. There has been also some studies where graphene has been synthesized directly on a dielectric surface, but the resulting graphene has been largely multilayered and the quality has not been very good [41, 42].

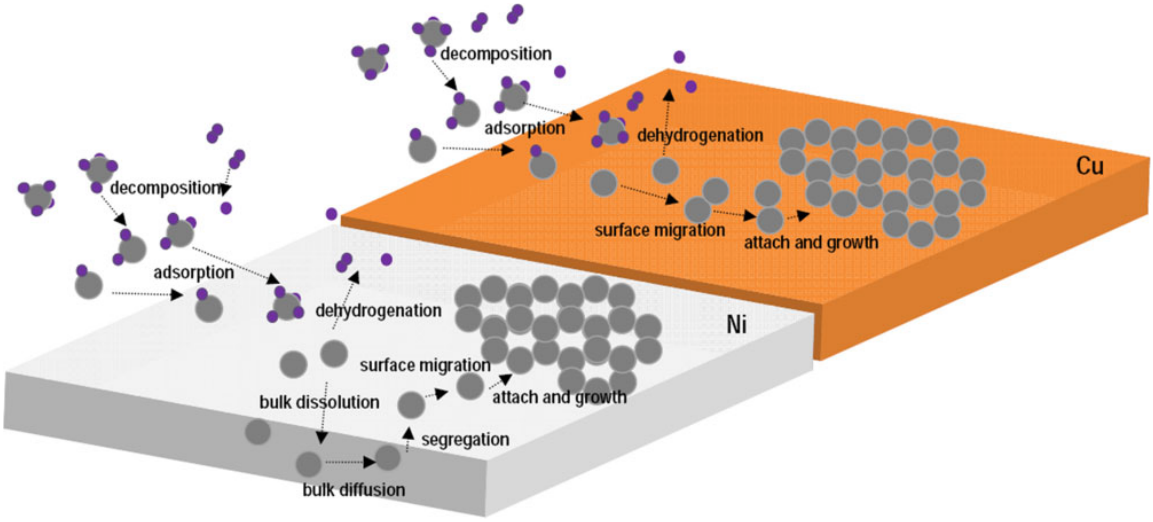

Figure 2: Schematic figure of CVD process on nickel and copper. [37]

The CVD process for nickel and copper is shown in Figure 2. Precursor gas in

CVD process is usually methane, but graphene synthesis has been demonstrated to work with other carbon compounds, such as alcohols [43] or solids [44]. Precursor is mixed with molecular hydrogen and many times also with argon to decrease carbon concentration. Argon dilution is used especially in atmospheric pressure growth.

The detailed mechanism of graphene synthesis is not completely known. The synthesis has been modeled only with methane precursor, as it is most common and a quite simple precursor [37]. As methane enters the reactor it can start to decompose already in the gas phase because of the high temperature, which is typically near or at 1000 °C. Mostly, though, dehydrogenation happens catalytically after adsorption. Once the precursor molecule adsorbs, the catalyst material determines what happens next. With nickel, carbon atoms or molecules undergo complete dehydrogenation, migrate on the surface and eventually form graphene. Also, as mentioned before, some carbon diffuses to the bulk and can precipitate to the surface afterwards. With copper catalyst the carbon most likely does not lose all the hydrogen atoms before reacting with other carbon atoms, according to first-principles DFT calculations [45]. In another computational paper it was found out that graphene might grow on copper through carbon dimers, which are stable and can migrate on copper [46]. Migrating carbon monomers, dimers, trimers etc. can then find each others and react to form graphene by first nucleating at some point and then growing from these domains by carbon attachment to graphene edges.

Points on the surface of catalysts where graphene starts to grow are called nucleation sites. These sites can be impurities on catalyst surface or crystal defects or boundaries [47, 48]. Ideally for high quality single layer graphene the number of nucleation sites is as low as possible, since less nucleation sites increases maximum size of graphene crystals because because of larger separation between them [49]. Therefore to decrease the number of nucleation sites and grow better graphene, high crystallinity and large grain sizes of catalyst are favorable. Also crystalline orientation of the catalyst affects the growth. For optimal growth conditions the catalyst surface should have hexagonal crystalline orientation, so that it aligns with graphene crystals. For metals that have fcc lattice, such as copper, this means that they should have the (111) surface on top. It has been found that Cu crystal orientation affects the shapes of graphene domains as well as the quality of them [50]. To fabricate a Cu(111) catalyst surface, one option is to deposit copper thin film on a single crystal substrate such as $\alpha - Al_2O_3(0001)$ [51]. The idea behind this is that during annealing $\alpha - Al_2O_3(0001)$ causes copper film to align itself with sapphire to form (111) surface, which improves graphene synthesis as mentioned above.

Before initiating graphene growth the copper surface is annealed usually at growth temperature. Annealing of catalyst is an important processing step, which cleans the surface, reduces oxides and improves crystallinity, all of which are processes that increase the quality of graphene [37, 49, 52]. For reducing and impurity cleaning purposes, the atmosphere usually contains hydrogen during this process. In general it can be said that longer annealing times and higher temperatures reduce graphene seeding and increase catalyst grain sizes, but these measures also promote evaporation of the catalyst material. When using thin film catalyst, longer times and higher temperatures can also enhance dewetting of the film [53].

After the annealing step the synthesis is started by introducing a precursor gas

to the chamber. The main parameters that affect the graphene CVD synthesis are total pressure, temperature, partial pressures, flow rate and duration of the growth step.

Graphene growth in various pressure ranges from atmospheric pressure all the way to high vacuum ($10^{-4} - 10^{-6}$ torr) have been studied quite extensively [54]. It is possible to synthesize monolayer graphene basically at any pressure, however the shapes of graphene domains are different, which indicates that there are differences in growth kinetics. With low pressure chemical vapor deposition (LPCVD) the domains are flower-like with either four or six lobed structures, whereas with atmospheric pressure CVD (APCVD) domains are predominantly hexagonal [54]. Furthermore, while with LPCVD graphene is mostly monolayered, with APCVD the number of layer is very much dependent on carbon precursor concentration [55]. With high carbon concentrations the grown graphene has monolayer spanning all over the sample with multilayer domains. Another important aspect with pressure is that low pressure causes the catalyst to evaporate/sublimate. This can be problematic especially with thin film catalysts if it causes dewetting. Evaporation puts some restrictions to pressure and temperature which are suitable for growth, but it is important to note that once graphene grows over the catalyst surface, it suppresses the evaporation [37].

Another very important growth parameter is temperature. Before growth the catalyst is heated at or near growth temperature. Growth temperature can vary depending on the catalyst material, but it is usually around 1000 °C, as mentioned before. It is however demonstrated that growths at even higher temperature (>1035 °C) decreases nucleation and therefore increases domain sizes, but it also increases problems with evaporation especially in LPCVD. However, there have been some studies where the synthesis has been performed on liquid catalysts [56], and there have been good results in this method including self aligned and fused graphene domains [57]. Since the growth temperature only gives enough energy for reaction to occur, it is not necessary to heat the whole reactor, but a "cold-wall" system is also possible, where only the sample is heated. Additionally there are many low temperature methods, which utilize some other way to activate precursor than thermal heat, such as plasma [58]. Low temperature methods could make graphene synthesis more feasible for industrial applications but thus far there has been only some success in producing large area single layer graphene with good quality [37, 58]. These methods could however become important in the future.

Graphene synthesis is affected greatly by concentrations of precursor and hydrogen gases and flow rate of gases. Hydrogen has many functions in graphene synthesis. It is used to clean the catalyst surface, reducing the surface from oxides and it also acts as a co-catalyst, but it also etches graphene [59]. The etching effect improves the graphene quality since it etches defective sites faster. Still it is possible to synthesize high quality graphene without hydrogen [60]. Usually hydrogen is also added to gas mixture in the annealing step to reduce any copper oxides on the surface, which could cause defects to graphene. There is however another method which relies on oxygen to reduce nucleation density and domain growth rate [61].

Effects of flow rate and concentration of precursor to graphene synthesis is however a bit more straightforward. Lower carbon flow and concentration decreases nucleation and helps to prevent multilayer graphene formation. With some recipes nucleation

is done with extremely small carbon concentrations to decrease the amount of nucleation centers, and after this the precursor flow is increased to achieve full sample coverage [62].

2.2.3 Electron beam lithography

Electron beam lithography (EBL) is a method that is widely used in nanoscale fabrication. This method is based on the use of resist polymers, which are polymers that react chemically when they are exposed to an electron beam. Depending on the polymer, the exposure can cause either formation of new bonds which causes more crosslinking, or it can cut chains in the polymer. Cutting bonds makes the resist more soluble to certain solvents and forming more bonds less soluble. By controlling which areas are exposed it is possible to create patterns in the nanometer scale.

Polymethyl methacrylate (PMMA) is a widely used resist in electron beam lithography, X-ray lithography and deep UV lithography. Electron beam exposure causes polymer chain scission, which makes it a positive resist. It is compatible with high resolution processing and can also be used for example as an etching mask. [63]

Lithography as a microfabrication process has several steps, which are shown schematically in Figure 3. The lithographic process begins by depositing the resist on the sample. With PMMA this is usually done by spin coating. In spin coating the PMMA is dissolved in a solvent such as anisole or chlorobenzene and a droplet of it is put on the center of the sample. Then the sample is spun at about 1000 to 5000 rpm, which causes the liquid to distribute very evenly on the sample surface. It is very important that the resist film has uniform thickness everywhere on the sample because if the thickness would vary, it could cause over- or underexposure. After spinning, the solvent is then evaporated either on a hot plate or in an oven. The thickness of the resist layer can be controlled with resist concentration, molecular weight and spinning speed.

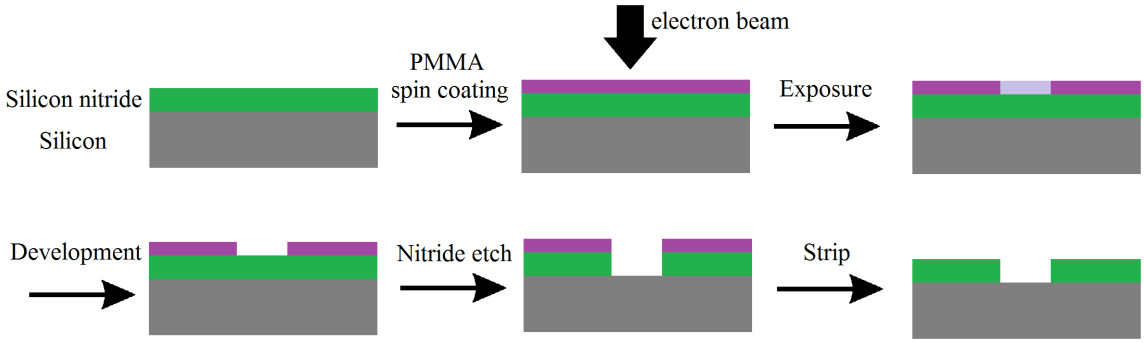

Figure 3: Lithographic steps with positive resist.

The exposure in electron beam lithography is done using patterns that are drawn using some CAD program. The pattern generator of the EBL system reads the file and scans the electron beam according to the predefined patterns.

After exposure the next step is development. With positive resists (e.g. PMMA) the exposed regions are dissolved and vice versa with negative resists. When using PMMA the developer is methyl isobutyl ketone (MIBK), which is usually mixed with isopropyl alcohol (IPA).

After development the sample is processed further. One way is to etch the underlying material, which means that the resist is used as an etching mask. This is presented in Figure 3. Another usual process is depositing material on the sample. After etching or deposition, the rest of the resist is washed away. This step where the resist is stripped is called lift-off, and with PMMA it is usually done by immersing the sample in warm acetone. Lift-off can also be enhanced for example by using an ultrasonic bath, but this might also result in damage to the pattern.

2.2.4 Etching

Etching is another important method in micro- and nanoscale device fabrication. It means removing material from its surface chemically, which can be done in many ways. Etching in microfabrication can be divided into dry or wet etching. Wet etching means that the process is done in solution and dry etching refers to etching that does not use liquid chemicals, such as plasma etching. Etching methods that are relevant to this work are Reactive Ion Etching (RIE) and silicon wet etching. [36]

Silicon can be wet etched in many ways but usually there is a need to do it in a controlled way. If silicon is crystalline, with certain etchants the etch rate depends on the crystal plane direction of silicon, i.e. the etching is anisotropic. One of the most used etchants in silicon etching is KOH, which etches the (100) crystal plane the fastest whereas the (111) plane etches slowly. This leads to the ethcing profile that can be seen in Figure 4. The etching rate is, of course, dependent also on the concentration of KOH and the temperature. The total reaction equation for silicon etching in alkaline solutions is [64]

$$\mathrm{Si} + 2\ \mathrm{OH^-} + 2\ \mathrm{H_2O} \longrightarrow \mathrm{SiO_2(OH)_2^{-2}} + 2\ \mathrm{H_2}. \tag{1}$$

Silicon nitride etches very slowly with KOH, making it a suitable material for an etch mask or for an etch stopper. By having a silicon wafer with nitride film on both sides it is possible to manufacture micro- or nanoscale windows by first etching a hole in the nitride on one side and then etching the silicon anisotropically. Once the window is ready it is also easy to make nanoscale openings in the window by lithographic patterning and etching holes in the nitride.

One of the most used dry ethcing method is Reactive Ion Etching (RIE). In RIE the material to be etched is placed in a vacuum chamber and the etching is done by reactive gases that are excited by a radio frequency (RF) signal. Usually one electrode is grounded and the other capacitively coupled to the RF-source. This causes electrode potentials to change so that the electrode connected to the source is at a much lower potential. The RF signal creates an electric field that accelerates electrons and ions between the electrodes. Collisions between particles inside the chamber cause both ionization and excitation of gas molecules, both of which are important. The sample is placed on top of the electrode which is coupled to the RF source (cathode), which increases ion bombardment. Ions that collide into the sample bring energy to the surface which may help the etching. In RIE however the main etching mechanism uses excited molecules which are very reactive. The idea in RIE is that the excited species react with the top molecule layer of the sample, forming a product which is very volatile and is desorbed from the surface. If the

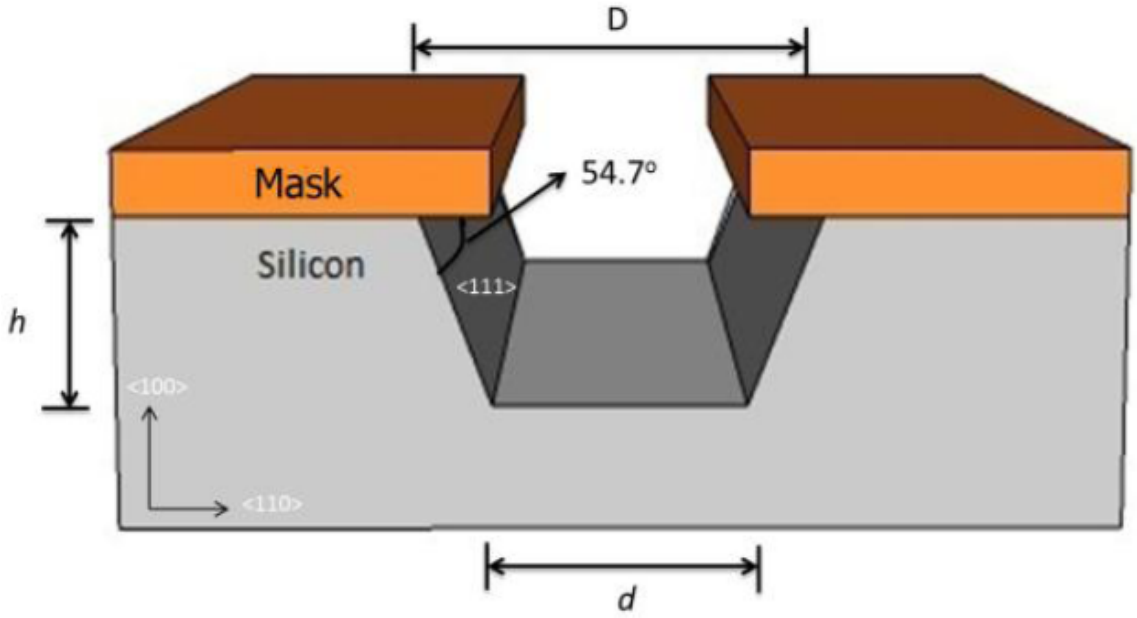

Figure 4: Anisotropic silicon wet etching profile. [65]

product is not volatile enough, it deposits on the surface and prevents etching. This layer can be sputtered with ion bombardment, but usually it leaves residues.

Anisotropy in plasma etching and RIE means vertical etching, which is caused by the directed particle bombardment. This means that by increasing the bombardment also anisotropy is increased. There are a few parameters, which are important in RIE and can affect isotropy and selectivity of etching. One of these parameters is the RF power, which affects to the DC bias and therefore the kinetic energy of accelerated particles. As the particles are accelerated towards the sample, if the RF power is increased, the collisions to vertical walls in the sample are decreased. Anisotropy can also be increased by decreasing pressure, increasing the amount of stabilizing gas and by substrate biasing.

Particle bombardment is an important part of RIE. Particles with high energy that hit the surface cause sputtering, which is a physical process. The etching is quite directional, but lacks selectivity compared to chemical etching, since selectivity comes from chemical reactions with the excited species. In pure plasma etching the plasma is only a source of excited molecules and ion bombardment is negligible. This is a highly selective process, but etching is isotropic. RIE is in between these extremes and the idea is to combine selectivity and directionality.

Silicon nitride, Si_3N_4, can be etched with many chemicals, such as SF_6, CF_4 and CHF_3, but SF_6 and CF_4 provide a isotropic etching profile and are not selective to silicon. CHF_3 is selective and can provide an anisotropic result. Often also small amounts of O_2 is introduced in the chamber to prevent the formation of a passivation layer. [66]

2.2.5 Graphene transfer and cleaning

Once graphene has been synthesized on the copper surface, it usually must be transferred onto another substrate. This process is very important for the final graphene quality. It is essential that the process does not cause any breaking of the graphene, such as tearing or folding. The transfer should also be as clean as possible, meaning that any residues or impurities should be cleaned.

A schematic image of the transfer process is presented in Figure 5. The first step in the transfer process is deposition of a support layer on the graphene. Mostly this layer is PMMA, which is applied on the sample by spin coating. After support polymer deposition the copper layer is etched away using an appropriate etchant. There are a few things one should keep in mind when choosing the etchant. First, it must be selective, so that it etches copper away effectively but does not harm the graphene. Secondly, it is good if the etching process does not form any gas bubbles under the graphene, such as hydrogen, which could be harmful. Finally, the etchant must not attack PMMA so that the support stays intact. There are plenty of different etchants that can be used for copper ethcing in this process. The most frequently used in publications is iron chloride ($FeCl_3$), but many others can be used, for example iron nitrate or ammonium persulfate [67].

Once the copper has been etched, the graphene/PMMA stack is rinsed with DI (deionized) water. At this point there is an opportunity to do additional cleaning steps. This cleaning can be an acid treatment or even modified RCA cleaning [68]. After cleaning is done, the sample is rinsed with DI water again and transferred onto the target substrate either by scooping the graphene/PMMA stack with the target substrate, or by draining the water away and letting the graphene settle on the substrate. The sample is then let to dry. To enhance the removal of water from between the substrate and the graphene, the sample can also be heated.

Next step is removal of the support layer, which is a critical part of the transfer process, especially when working with suspended graphene. With more common samples, i.g. graphene transferred onto normal SiO_2 surface, the support layer is removed by dissolving it with acetone or chloroform. However, because suspended graphene is quite fragile, it is important to have a gentle method for support layer removal with suspended graphene. With the normal removal method the sample chip is inserted in and pulled out from a solvent bath, which can damage suspended graphene just because of the surface tension. More gentle methods include thermal annealing and critical point drying, which is described in section 2.2.6. Thermal annealing is a dry method, in which the graphene sample with PMMA is heated to $200 - 400$ °C, which causes the PMMA to decompose.

A very common problem with CVD graphene is that impurities remain on the graphene after transfer. These are either residues from the support layer, the copper or the etchant. Metallic impurities are demonstrated to be removable using above mentioned acid treatments. However residues from PMMA support are more difficult to remove. Numerous different methods, such as thermal annealing [69], plasma cleaning [70] and UV irradiation [71], have been proposed to solve the PMMA residue problem.

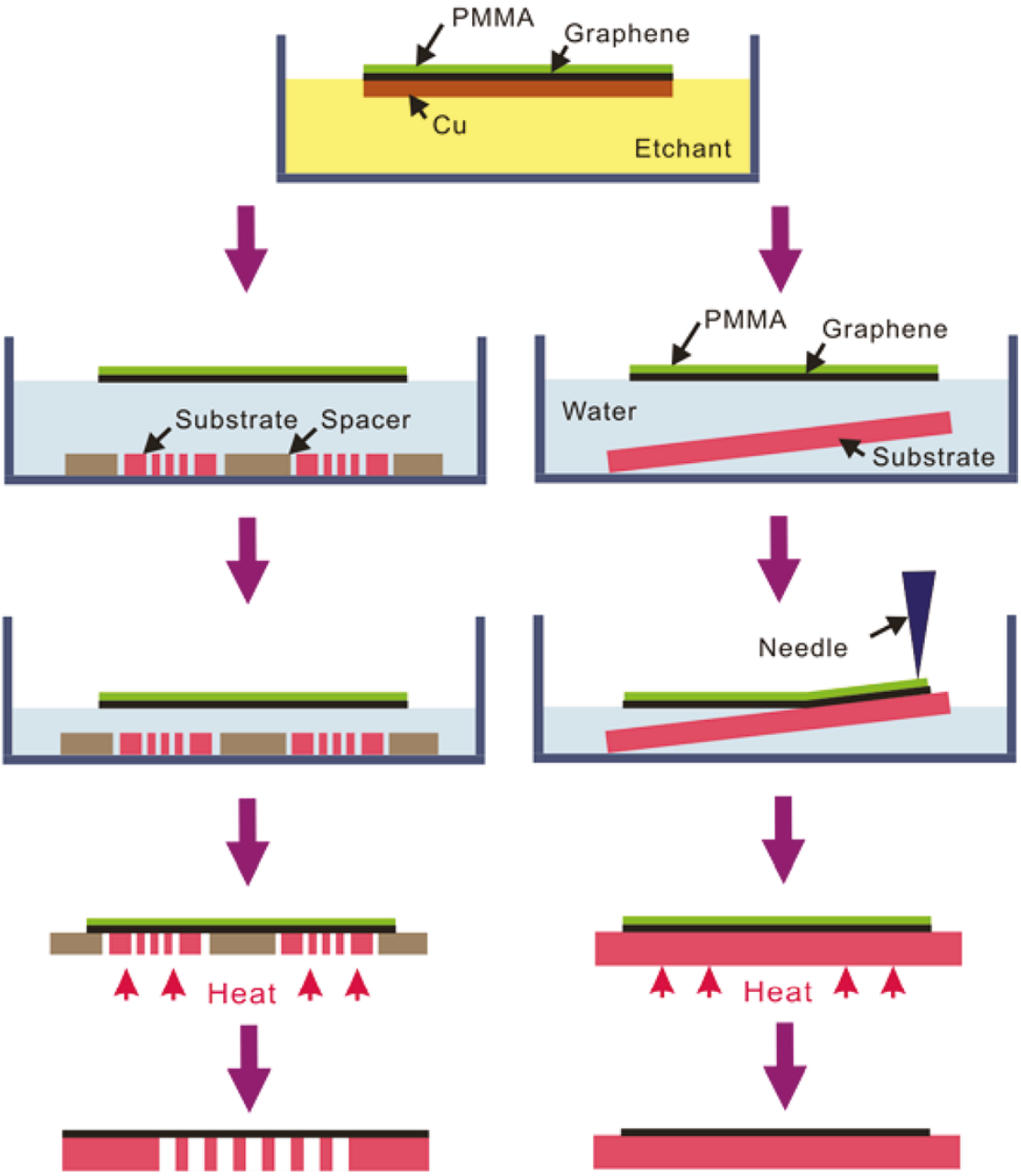

Figure 5: An illustration of the transfer process [72].

2.2.6 Critical point drying

Critical point drying (CPD), or supercritical drying, is a technique for drying fragile samples. It is used widely in the field of biology to prepare for example tissue samples to scanning electron microscopy, and also in the production of microelectromechanical systems (MEMS).

In normal drying the sample is pulled out of the liquid or the liquid is evaporated away, but the surface tension during these steps can destroy a fragile sample. In CPD the sample is dried without crossing a phase boundary by going around the critical point from liquid through supercritical fluid to gas. There are only a few suitable fluids that have their critical point at low enough temperature and pressure to be useful in CPD. Nowadays carbon dioxide (CO_2) is the most commonly used fluid for CPD [73]. Other possibilities would be nitrous oxide or Freon 13, but they are more problematic to work with and they are more expensive.

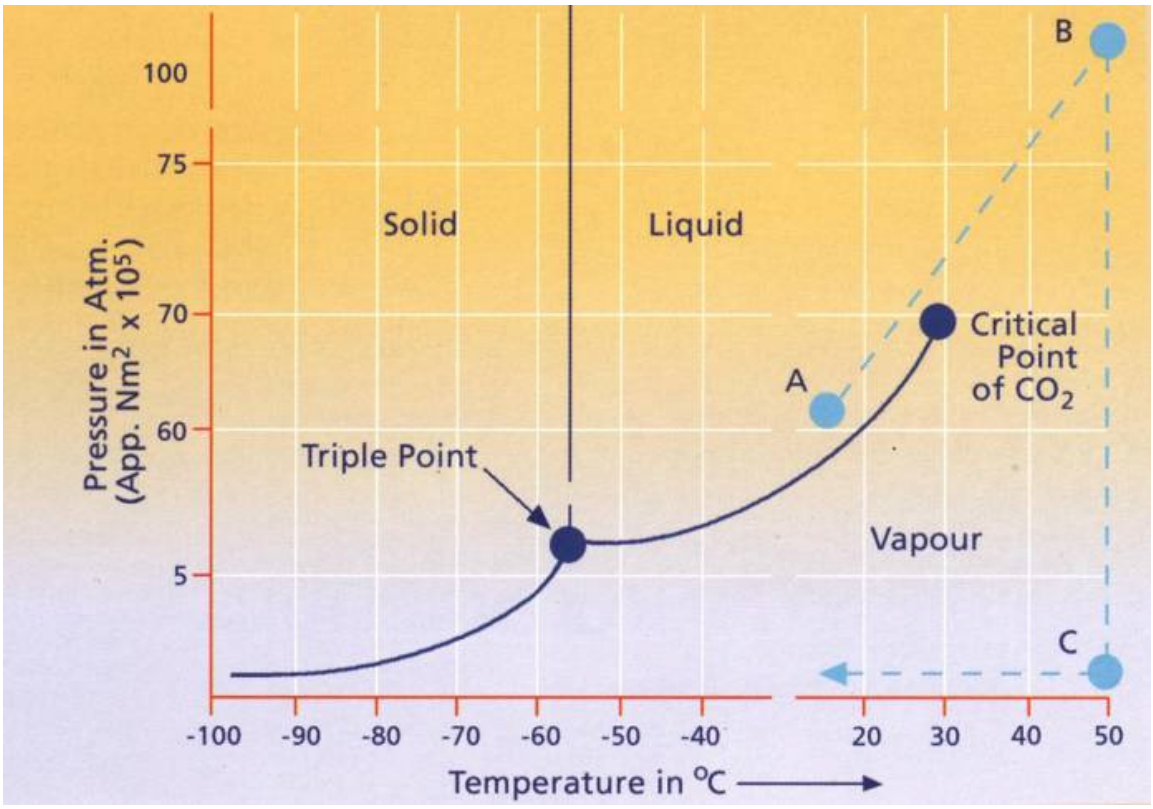

Figure 6: Phase diagram of CO_2. [73]

The CPD process is presented in the phase diagram of CO_2 in Figure 6. The process starts from ambient conditions at point A. When performing the process, first pressure is increased and then temperature to reach point B. These can be done also simultaneously since heating a closed chamber also increases the pressure inside it. At point B the state of the fluid is past the critical point, and liquid and gas have the same density and are indistinguishable, forming a homogenous fluid. This eliminates the surface tension and also any forces that could harm the sample. Once the fluid is in the supercritical state, the pressure is reduced slowly until point C

(ambient pressure) is reached, and finally the chamber is cooled. The fluid has then become gas without crossing a phase boundary.

2.3 Electron microscopy

2.3.1 Principles

Electron microscopes use an electron beam to image a sample. Electron microscopes allow much higher magnifications compared to optical microscopes, which are diffraction limited to about half of the wavelength of light [74]. Electrons have about five orders of magnitude smaller wavelength, making much higher magnification possible. Electron microscopes are however analogous to optical microscopes in the sense that they both have a column with electron or light source and condenser and objective lenses that work similarly. One of the main differences is that electron microscopes require vacuum to prevent electron scattering. [75]

The electron beam, which is used in imaging, is generated on top of the column by an electron gun. To generate electron emission, electrons must be given enough energy to overcome the work function, which can be done in many ways. The simplest way to create an electron beam is to use thermal emission, where the electron source filament is heated to high enough temperature that electrons can escape. The electrons are accelerated from the gun (cathode) to the sample (anode) but this potential difference does not have an effect on the emission itself. Usually the filament is covered by a Wehnelt electrode, which is a metal cylinder with a small hole for the electron beam. The Wehnelt is put to more negative potential than the cathode to decrease the emission area, which helps to control the emission current [74]. The filament material has to be stable in vacuum at high temperature, which is why tungsten is a usual material for filaments. Tungsten has, however, a quite high work function, which is not ideal. Another often used material in thermal emission electron guns is lanthanum hexaboride (LaB_6), which has much lower work function compared to tungsten. The LaB_6 source is shaped as a sharpened rod and the emission occurs from the very tip of it. Because electrons are emitted from a smaller area, the beam can also be focused more precisely. Additionally, this also causes better brightness. The drawback is that LaB_6 is more expensive and easily reacts with any traces of oxygen, which means that vacuum needs to be better compared to tungsten filament.

By applying an electric field to a V shaped cathode, the work function can be decreased, which increases the emission current density. Heating is also required to achieve emission, but the temperature is lower than in pure thermal emission. This type of emission is Schottky emission or thermal field emission. The cathode material is tungsten covered with zirconium oxide (ZrO), which has a low work function but it is also very sensitive to any gases. This means that ZrO demands better vacuum level compared to tungsten or LaB_6 sources.

A third emission method is field emission, in which the electric field near the cathode is increased so much that electrons can escape via quantum mechanical tunneling. The cathode tip is sharpened to be very thin, which helps the tunneling and also causes the electrons to be emitted from a very small area, which makes the beam easier to focus. Field emission sources have quite long lifetime since the source is not heated at all. The electron beam generated with this method also has a high

current density and brightness compared to previous methods. The drawback with this method is that the system is quite expensive, since ultra-high vacuum is required for its operation.

After the electron beam is generated, it must be focused. This is done in the column by using electron optical lenses. These lenses are usually electromagnetic lenses, which use a magnetic field produced by a wire coil carrying current. As electron moves through this magnetic field, it is deflected according to Lorentz force

$$\vec{F} = -e\vec{v} \times \vec{B}, \tag{2}$$

where $\vec{F}$ is the force that the electron experiences moving through the magnetic field. Here e is the elementary charge, $\vec{v}$ the velocity of electrons and $\vec{B}$ the magnetic field. The principle of electron lens focusing is presented in Figure 7.

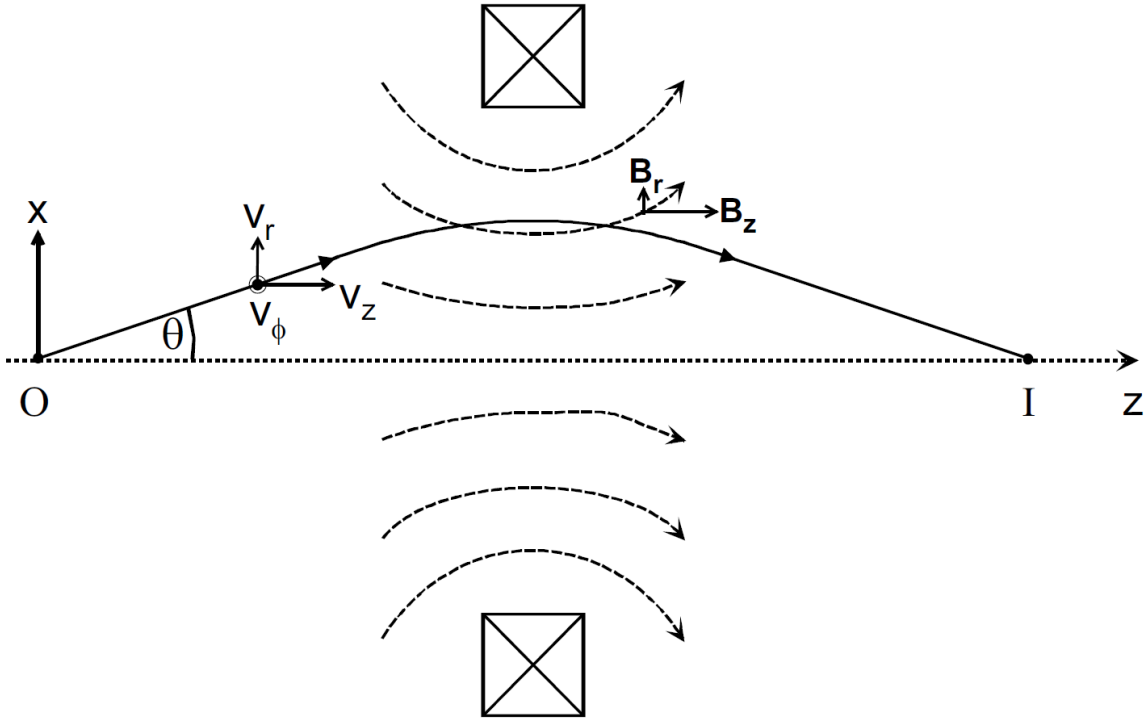

Figure 7: Magnetic lens [74].

Aberration in magnetic lenses are also similar compared to optical lenses. Common aberrations are astigmatism, spherical aberration and chromatic aberration. Astigmatism is caused if the lens not completely circular or if the magnetic field caused by it is not radially uniform. This causes the electron beam cross section to become an ellipse instead of a circle, which distorts features in the image. Astigmatism can be corrected with correcting lenses. Spherical aberration is caused when the lens refraction is different in the center and on the edges. This causes electrons passing different parts of the lens to have different focal point. Chromatic aberration happens when electrons with different kinetic energy are focused in different focal point. Differences in energies of electrons can be caused by an energy spread of the

source, by fluctuations in acceleration voltage and by scattering. Spherical aberration and chromatic aberration can be decreased by having stronger lenses, high acceleration voltage and apertures. Apertures are used to block the outer part of the beam, which makes focusing of the beam easier, but also decreases brightness and beam current.

2.3.2 Transmission electron microscope

In a transmission electron microscope (TEM) the electron beam is used to illuminate the sample and detect electrons that transmit through it. The working principle of TEMs is very similar to optical transmission microscopes. The parts of a TEM are presented in Figure 8.

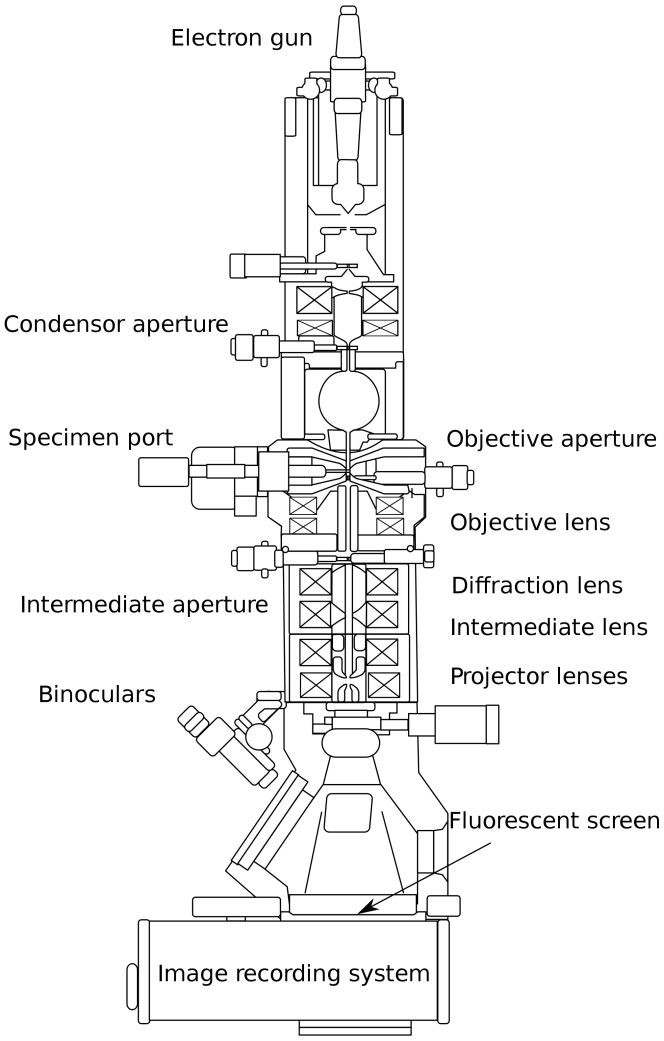

Figure 8: Schematic of a TEM [76].

The electron beam is generated at the top of the column and is directed through the condenser lens system. Condenser lenses are needed to ensure good brightness of the final image even with high magnifications. This system consists of at least

two lenses and one aperture. The condenser lenses focus the beam on the sample and their strength is changed when illuminated area is changed. After the electrons move through the sample, they arrive to the objective lens, which causes most of the magnifying power. There are many lenses between the objective lens and the final projector lens, which have different functions. Intermediate lenses allow the change of magnification and making of diffraction pattern. The final lenses of the TEM are the projector lenses, which are used to expand the beam to centimeter scale for final image. To transfer the electron radiation to visible light, the screen which the beam is projected on is fluorescent. Nowadays the imaging is done using a phosphor screen and a CCD camera, which allows electronic recording of images.

In transmission electron microscopy the electron beam is directed to a very thin sample. Some parts of the sample absorb or diffract more electrons than others, which enables the image formation. Since the electrons must travel through the sample, it must be very thin, which brings limits to the useability of TEM. Samples that are not thin must go through lots of preparation to make them suitable for TEM imaging. Once a sample is thin enough, the TEM allows extremely high magnifications, even to atomic scale resolution [74]. For this reason it is widely used to image nanosized particles or structures.

2.3.3 Scanning electron microscope

The scanning electron microscope (SEM) can be seen analogous to optical reflection microscopes. A schematic image of a SEM is presented in Figure 9.

The electron beam hitting the sample surface causes several different processes. Electrons can scatter elastically or lose some energy in the scattering process, and these backscattered electrons can be used in image formation. Primary electrons can also excite atoms and/or molecules in the sample and cause X-ray emission or cathodoluminescence, which can be used for sample characterization as well. In conventional scanning electron microscopy the image is, however, created by detecting secondary electrons.

These secondary electrons are generated when incident electrons from the beam hit the sample surface and have inelastic interactions with the material and cause emission of low energy electrons. Because the electrons have low energy, they cannot travel a long way inside the sample and therefore the detected electrons come from a few nanometer depth of the sample. Also, since they have low energy, secondary electrons can be collected using positive voltage which does not affect the high energy backscattered electrons. The collected electrons are converted to electric signal and amplified. The signal is then sent to a cathode ray tube for image formation, or in more modern devices, the signal is converted to a digital signal and the image is formed on the computer screen. The image is formed by scanning the sample with the beam and measuring the intensity of secondary electron emission at each point. Using secondary electrons in imaging is useful since the electrons are emitted to all directions and the image that is formed does not have shadows.

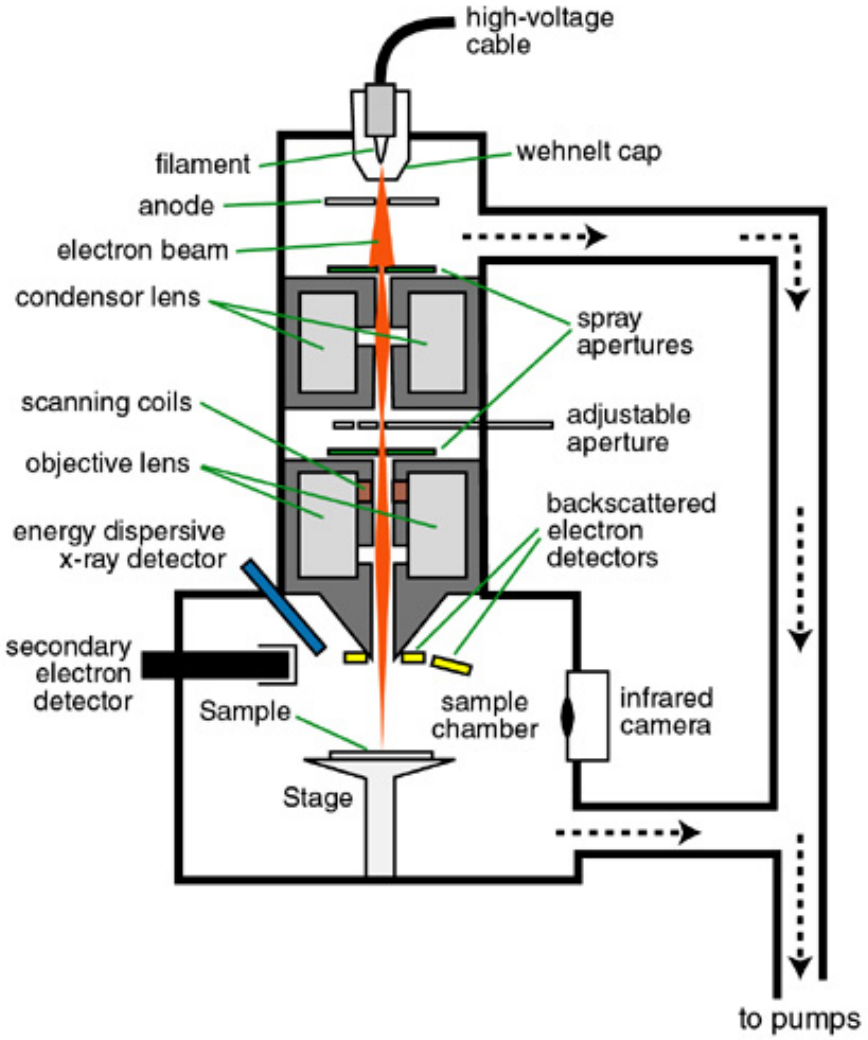

Figure 9: Schematic of SEM [77].

2.4 Raman spectroscopy

Raman spectroscopy is a widely used method to find the chemical composition of samples. This is based on a Raman spectrum giving information about the sample's characteristic vibrations of chemical bonds or groups [78]. Raman spectroscopy has been used for a long time to study carbon nanotubes and Raman spectroscopy quickly became one of the most important methods to characterize graphene as well.

In Raman spectroscopy the sample is irradiated with monochromatic light, usually from a laser. The sample absorbs some of this light, causing the excitation of electrons to higher energy states. As electrons relax from higher to lower state they emit a photon which energy corresponds to the energy difference between the states, ΔE, by an equation:

$$\Delta E = E_p = h\nu, \tag{3}$$

where E_p is the energy of the photon, h is Planck's constant and ν is the frequency of the photon [78]. Usually in Raman spectroscopy the transitions are presented in

wavenumbers instead of frequency or wavelength, which are related by an equation:

$$\bar{\nu} = \frac{\nu}{c/n} = \frac{1}{\lambda}, \tag{4}$$

where $\bar{\nu}$ is the wavenumber, c is the speed of light, n is the refractive index of the medium and λ is the wavelength. The unit of wavenumber is usually written as cm^{-1}.

A photon can be scattered in a few different ways when it hits the sample. The basic idea of Raman scattering is displayed in Figure 10. The most common process is Rayleigh scattering where the photon scatters elastically without changing energy and therefore wavelengths of the incoming and the scattered photons are the same. A majority of photons scatter via Rayleigh scattering. When scattering is inelastic, incident and scattered photons have different energy. This is called Raman scattering. There are two types of Raman scattering: Stokes and anti-Stokes. In Stokes Raman scattering the molecule is initially in the ground vibrational state and excited to virtual state, after which it relaxes to some other vibrational state, so the scattered photon has lower energy than the incident photon. In anti-Stokes, the molecule is at an excited vibrational state and ends up in a lower excited or ground state, so the scattered photon has higher energy. Anti-Stokes signal intensity is usually much lower compared to Stokes, since usually there is only small population at an excited state at ambient conditions [78].

The change of wavelength in scattered light is dependent on the sample molecule. Different materials and different structures scatter light differently, which makes Raman spectroscopy an extremely useful approach when analyzing chemical substances and structures of samples. In the case of graphene, Raman spectroscopy is also a very convenient analysis method, being nondestructive and a fast way to examine the quality of graphene.

A usual practice in Raman spectroscopy is to present the spectrum as wavenumber shift (Raman shift) from the Rayleigh peak. Graphene has three main bands in its Raman spectrum: D, G and 2D. The G band is originating from stretching of bonds between sp^2 carbon atoms and the location of it is at $\sim$1580 cm^{-1} [79]. The D band, which is at $\sim$1350 cm^{-1}, is present when there are defects in the graphene lattice. The origin of this band is related to breathing modes of carbon atom rings [80]. The third peak in the graphene spectrum is the 2D peak at $\sim$2700 cm^{-1} [81, 82]. This peak is historically called G' since it is the second most prominent peak in the Raman spectrum of graphite. It is also called the 2D band because it is the second order of the D band. With monolayer graphene the 2D peak is composed of a single peak, but with bilayer or few-layer graphene the band consists four peaks [83]. This causes the 2D peak to be high and sharp with monolayer graphene and broader and less intense when the number of layers increases. Because of this, it is possible to evaluate the number of layers by comparing the 2D intensity to the G intensity.

It is possible to measure the Raman spectra of graphene directly on a copper surface. This is a fast way and practical way to do basic characterization and analyze whether the growth was successful or not. Photoluminescence of copper causes the Raman spectrum to have a very broad band at the same region that the carbon peaks mentioned above are [84].

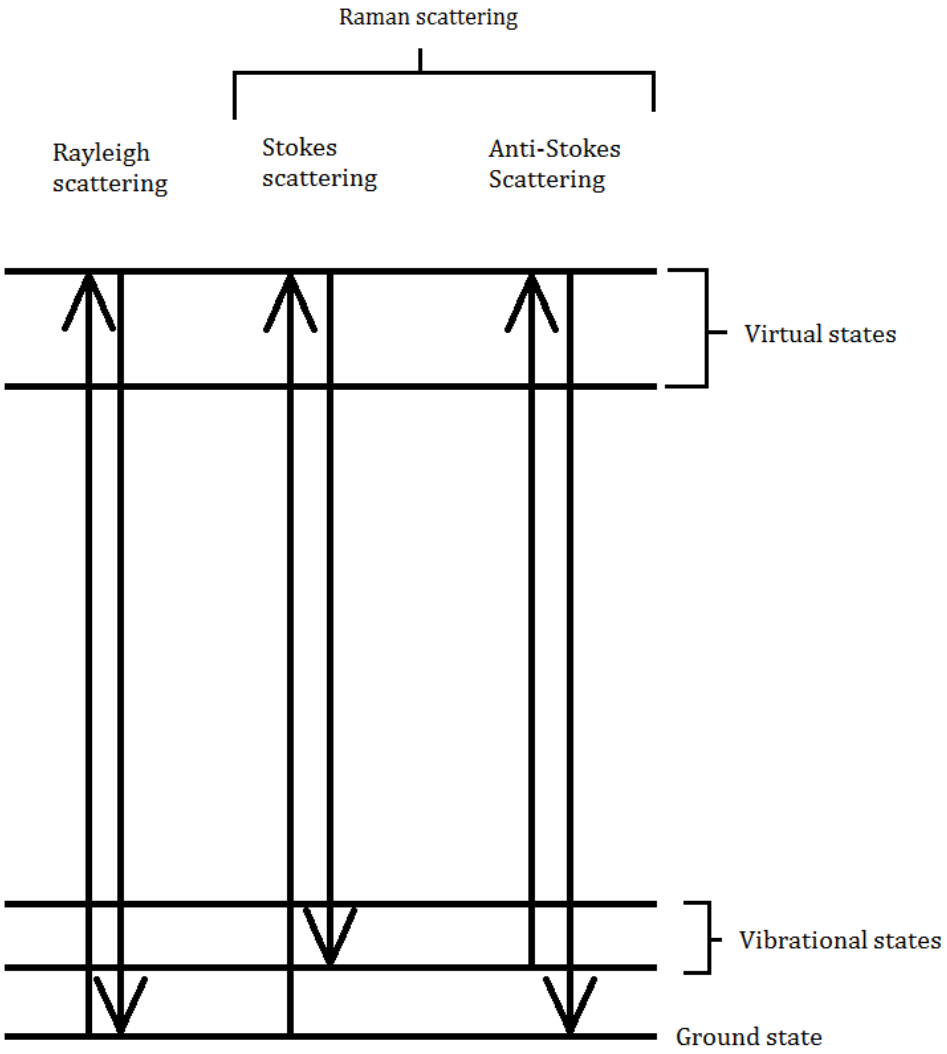

Figure 10: Basic Raman transitions

3 Experimental section

3.1 Sample fabrication

3.1.1 Silicon nitride grid fabrication

Silicon nitride grids were fabricated from an intrinsic (100) silicon wafer with two sided 300 nm thick nitride film. A schematic image of the fabrication steps is presented in Figure 11. The processing started by patterning a large square pattern on one side of the chip. The patterning was done using electron beam lithography. First both sides of the chip were cleaned well with warm acetone, rinsed with IPA (isopropanol alcohol) and dried with N_2 gun. Then one side of the chip was spin coated with 950 PMMA A11 (Poly(methyl methacrylate) with molecular weight of 950 000 dissolved in anisole 11 m-%) at 4000 rpm and baked for three minutes on a hot plate at 170 °C. Next the patterns were exposed using Raith eLine SEM/e-beam lithography tool with 700 $\mu As/cm^2$ charge dose, followed by development in MIBK(methyl isobutyl ketone)/IPA 1:3 for 60 seconds. After the patterns were developed the exposed nitride regions were etched using a RIE process. The etching was performed using Oxford Instruments Plasmalab 80 Plus with gas flows of 50 sccm CHF_3 and 5 sccm O_2 at 30 °C temperature, 55 mbar pressure and with power of 100 W for 15 minutes. Then rest of the PMMA was washed away with acetone, and silicon was etched using KOH wet etching method. Silicon was etched for a few hours in 35 % KOH solution while temperature was held at about 99 °C. After silicon was etched, the samples were rinsed in four consecutive baths of DI water and blown dry with N_2 gun.

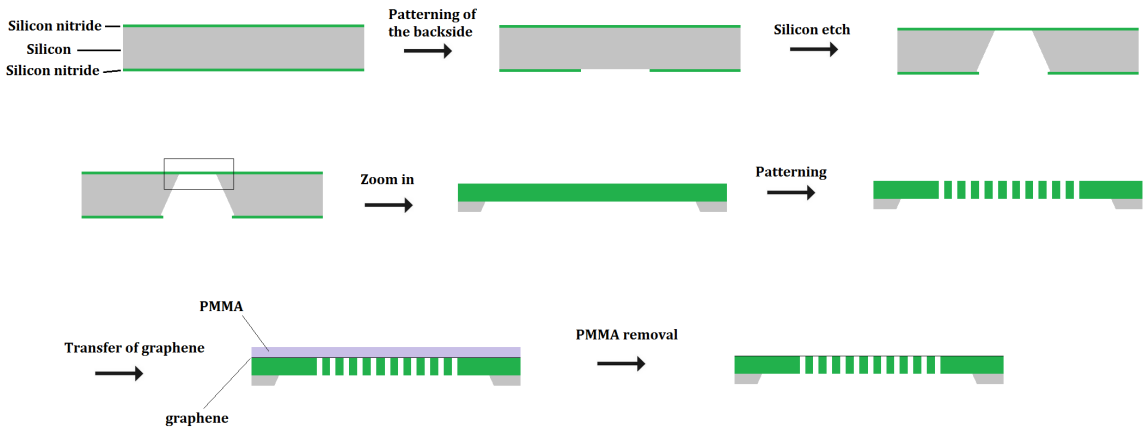

Figure 11: Fabrication of Si_3N_4 substrate and graphene transfer.

Once the Si_3N_4 membrane windows were fabricated, openings in them were done using the same methods as previously. First 15 nm of copper was deposited onto the window side of the chips to form a conductive layer. This was done using a modified Baltec BAE 250 evaporator. Then chips were coated with 950 PMMA A2 at 4000 rpm and baked for 2 minutes. Then opening patterns were exposed also with eLine using 300 $\mu As/cm^2$ dose and developed in MIBK/IPA 1:3 for 50 seconds. After

this copper was etched from exposed areas by immersing sample into copper etchant for two seconds. The solution was H_2O:$C_2H_4O_2$:H_2O_2 in ratios of 18:1:1. Then the rest of the PMMA was washed away using hot acetone, which was followed by nitride etching using same method and parameters as before. Finally the rest of the copper mask was etched away, leaving only the suspended nitride grid.

The opening patterns were arrays of circles. Four different diameter sizes were tested: 7 µm, 10 µm, 15 µm and 20 µm.

3.1.2 Graphene synthesis

The first step in our graphene synthesis was fabrication of the copper catalyst surface. A wafer of single crystal α-Al_2O_3 (sapphire) with (0001) surface was cut to 5 mm × 5 mm chips. After this 600 nm of copper was evaporated onto the sapphire chips using, as previously, Baltec BAE 250 electron beam evaporator at a pressure of 10^{-5} mbar with a deposition rate of 5 Å/s.

Graphene synthesis was done in MTI GSL-1100X 2" quartz tube furnace using ethanol as precursor. The sample holder was a small open ended quartz tube that was attached to a steel rod, which also held a thermocouple for temperature readings. A schematic image of the setup is shown in Figure 12. First in the synthesis procedure the as fabricated catalyst films were annealed at growth temperature (usually 1000 °C) and at atmospheric pressure of an Ar/H_2 gas mixture to reduce copper oxides and to improve the crystallinity of the films. Synthesis was initiated by diverting part of the gas flow into the precursor (ethanol) bubbler. Growth was terminated by closing gas flow to the bubbler and pulling the samples out of the furnace hot spot. The samples were cooled in Ar/H_2 atmosphere until their temperature was under 200 °C to prevent oxidation from oxygen in air.

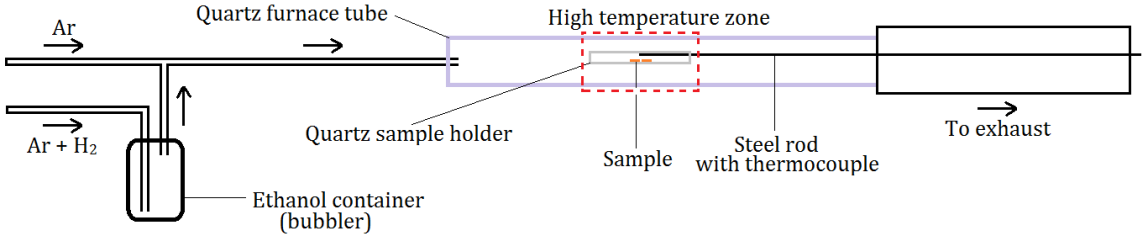

Figure 12: Schematic view of CVD setup.

3.1.3 Transfer and cleaning

After synthesis the graphene was transferred onto silicon nitride grids. First the graphene was covered with PMMA and the copper was etched away under the graphene. Etchant for this was at first iron chloride ($FeCl_3$), but it was later changed to ammonium persulfate because of concerns with incompatibility with iron chloride and PMMA [67]. The copper ethcing left the PMMA/graphene stack floating on the etchant bath. The stack was then scooped from from the etchant bath and placed into four consecutive DI water baths for rinsing. Then the stack was moved to a 10 % hydrochloric acid bath for 5 minutes to clean possible ionic residues. After this the stack was moved again through four DI water baths. Then the silicon nitride grid was placed on the bottom of the last water cup and water was pumped slowly away, while directing the PMMA/graphene stack using tweezers. Once the stack was placed onto the nitride grid, the sample was dried using hot plate to drive away any water left between graphene and the nitride film.

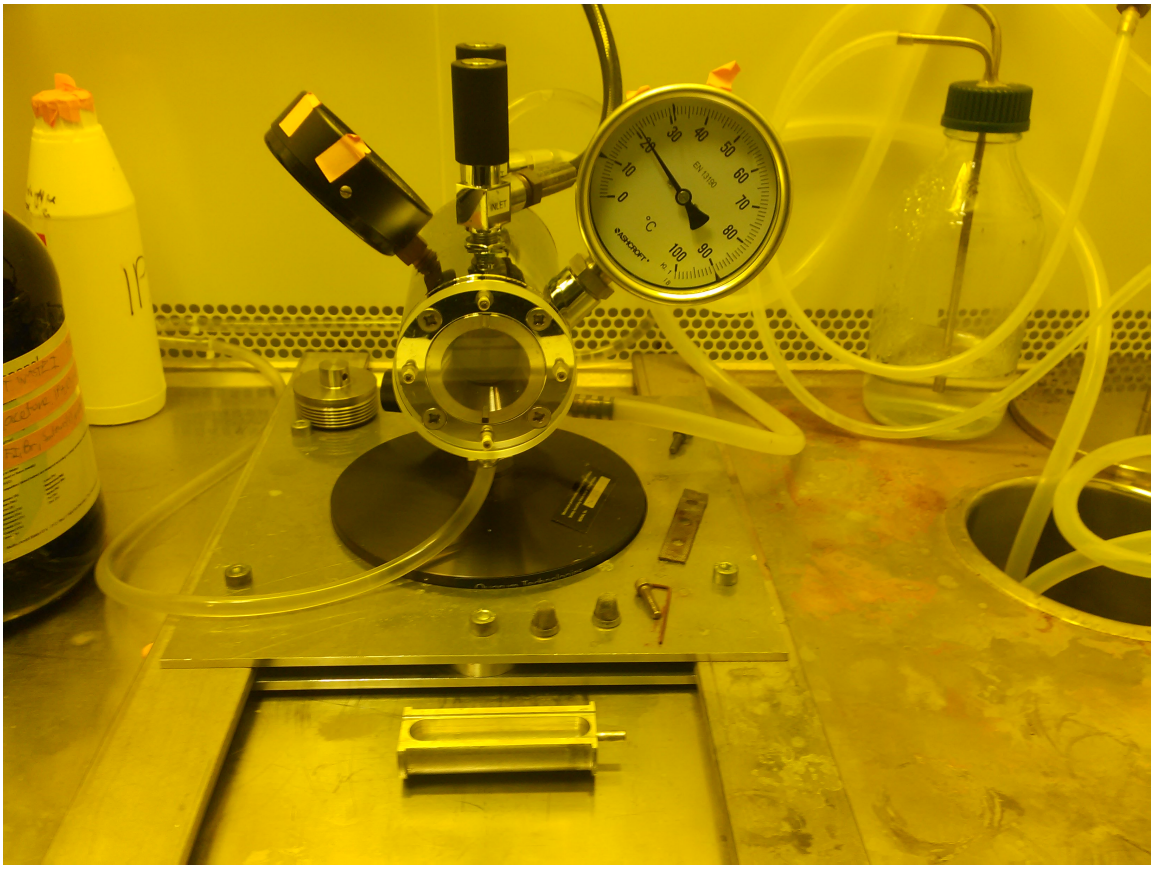

Figure 13: An image of the CPD setup used in this work.

After the transfer process the PMMA layer was removed. This was done using two different techniques, annealing and/or critical point drying (CPD). With annealing the used furnace was a Carbolite CTF 12/65/550 with an Eurotherm 3216 temperature/process controller. The effect of temperature was tested by annealing different samples in the temperature range of 200-400 °C. Annealing was tested in both N_2 and O_2. The other PMMA removing method was CPD, which was done

using a Quarum Technologies E3000 critical point drying apparatus, shown in Figure 13. In the process a metal boat was filled with acetone and samples were immersed into it and left for 5-10 minutes, so that acetone dissolves the PMMA layer before loading the boat into the pressure chamber. After this acetone was changed to liquid CO_2 and the chamber filled about half full with it before heating the system to about 40 °C to bring the temperature clearly above the critical temperature of CO_2, which is 31 °C. This temperature rise also increased pressure to over 80 bar, which is higher than the critical pressure of 75 bar. Once the required temperature and pressure were reached and the phase boundary between liquid and gaseous CO_2 inside the chamber had disappeared, the chamber was slowly vented to atmospheric pressure.

3.2 Characterization

The samples were characterized using a Raith eLine scanning electron microscope with 2 kV acceleration voltage, shown in Figure 14a.

Transmission electron microscopy was done using a Jeol JEM-1400 microscope with 80 kV acceleration voltage and a LaB_6 source, shown in Figure 14b.

Raman measurements were done using a home built system in backscattering geometry, shown in Figure 14c. The excitation laser used was a 532 nm wavelength Alphalas Monolas-532-100-SM and the beam was focused using a Nikon L Plan SLWD 100x microscope objective with 0.70 N.A. The used spectrograph was an Acton SpectraPro 2500i 0.5 m imaging spectrograph using 600 g/mm grating. Signal detection was done using an Andor Newton EM DU971N-BV EMCCD camera with a slit width of 100 µm. The Rayleigh peak was attenuated using a Semrock edge filter and sample positioning was done using a Newport ULTRAling 462-XYZ-M manual stage.

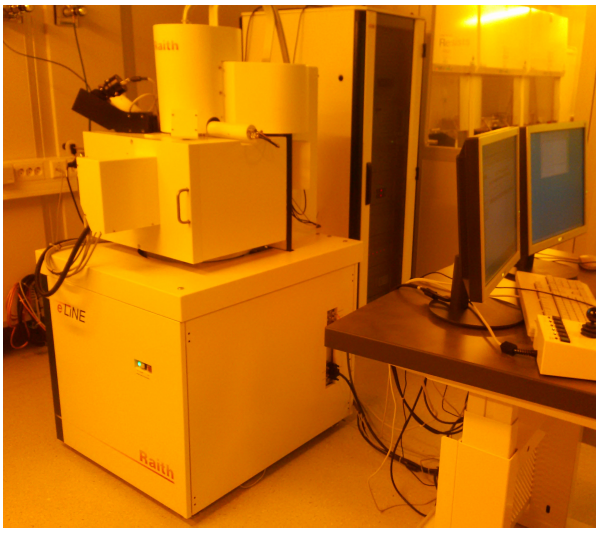

(a) eLine SEM

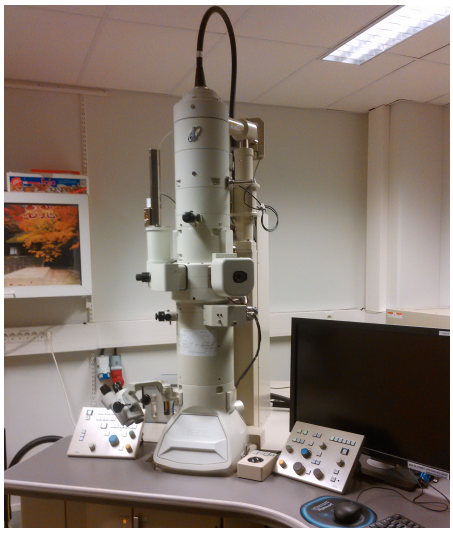

(b) JEOL JEM-1400 TEM

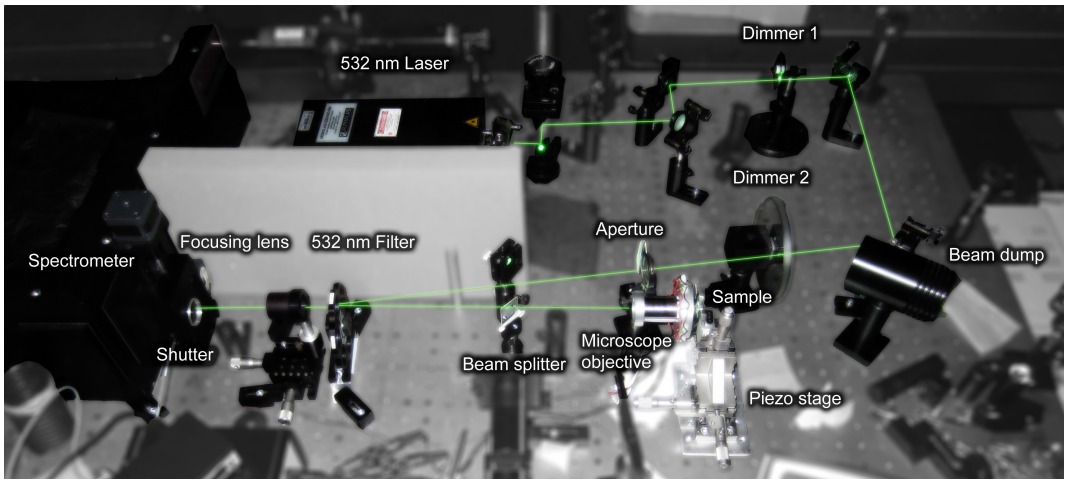

(c) Raman setup

Figure 14: Photographs of SEM (a), TEM (b) and Raman (c) setups used in this thesis.

4 Results and discussion

4.1 Effect of copper grains to synthesized graphene

In the first part of the experimental work a copper catalyst surface was fabricated by electron beam evaporation onto monocrystalline Al_2O_3 substrates, as it was described in [51]. A collection of optical microscope (OM) images from different samples is shown in Figure 15. In Figure 15a an OM image of a freshly evaporated copper surface is presented. In Figures 15b, 15c, 15d, 15e and 15f are different kinds of patterns that appear on copper when it is annealed in high temperature (1000 °C). Samples in Figures 15b, 15c, 15d and 15e were annealed under 20 sccm H_2 and 250 sccm Ar flow for 20 minutes, which was followed by a growth phase by diverting 100 sccm Ar and 30 sccm H_2 through bubbler and diluting it with 470 sccm more Ar. Growth time was 20 min and temperature 1000 °C, so the samples were at high temperature total of a 40 min. The sample in Figure 15f was annealed under 50 sccm H_2 and 50 sccm Ar flow for 30 minutes, which was followed by graphene growth using 20 sccm of Ar and 20 sccm H_2 as the bubbler flow and 560 sccm Ar as the dilution for 5 min. The temperatures under annealing and growth were 1000 °C.

From Figure 15a it can be seen that after evaporation the copper surface is clearly smooth and featureless except a few small impurities. Figure 15b shows a sample where copper has arranged to small domains, except a large domain on the right top corner, with clear grain boundaries between them. In Figure 15c some of the copper grains are larger and some of the grain boundaries are not as clear. Figure 15d is an image of copper with huge grain size. The image is taken from a spot where one of the few grain boundaries is visible, but otherwise the majority of the 5×5 mm surface is the same grain. Figure 15e has copper that has one large domain that is spotted by small domain islands. The last image in Figure 15f has two distinctive regions, on upper part many small domains are separated by grain boundaries and on the lower part copper seems to be continuous over a large distance, and between these regions is a more clear and deep boundary than those on the upper region. Black round spots in Figures 15b, 15e and 15f are spots where copper has dewetted. The fact that copper completely reorganizes was an expected result from previous work and reports from others [85, 53]. It was also found in [85] that sapphire does cause copper to have (111) crystal plane surface and that annealing increases crystallinity and smoothness of copper.

In an article by Miller *et al.* [53] the copper has very similar thermal groove patterns compared to those in Figure 15. In this work all depositions were done at room temperature, whereas they heated the substrate during deposition. They found that copper deposition temperature made a big difference in copper grain size after annealing. In this work, however, many of those patterns are visible in different samples even tough copper films were deposited only at room temperature. Actually there can be even many different patterns in the same sample. Additionally, the thermal groove structure that they had for their sample that was deposited at 25 °C was not found at all in this work. It is also important to note that deposition and annealing were a bit different in the work of Miller *et al.* They deposited copper by sputtering and their film thickness was $450 - 500$ nm, whereas in this work copper

(a) Copper after evaporation

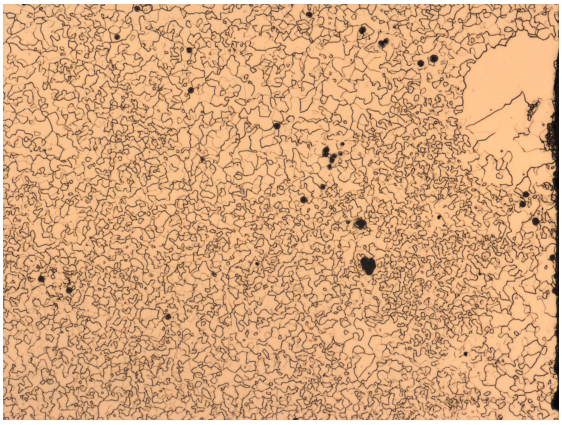

(b) After annealing and synthesis

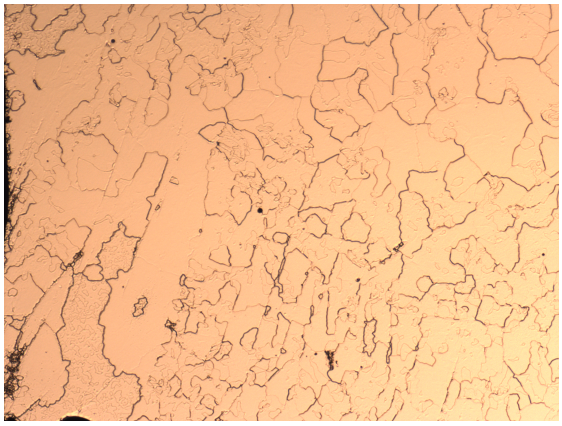

(c) After annealing and synthesis

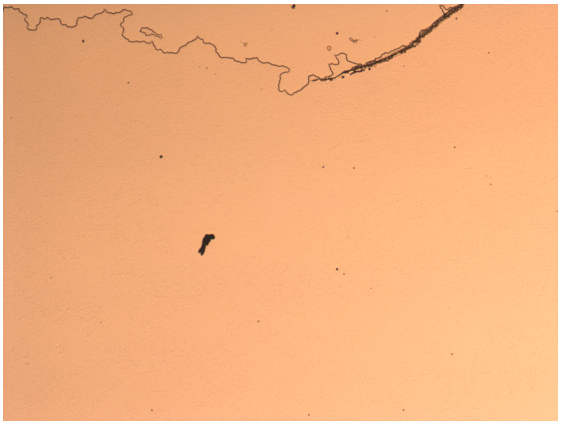

(d) After annealing and synthesis

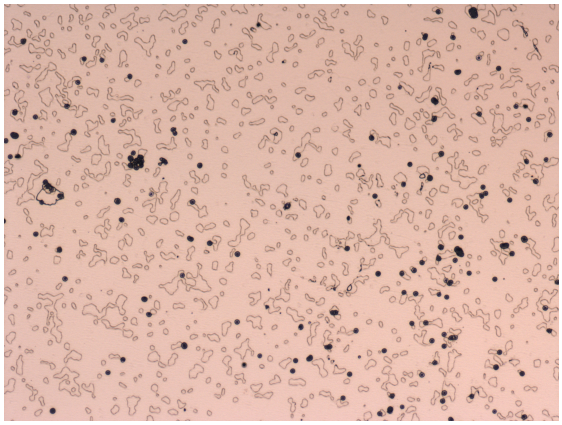

(e) After annealing and synthesis

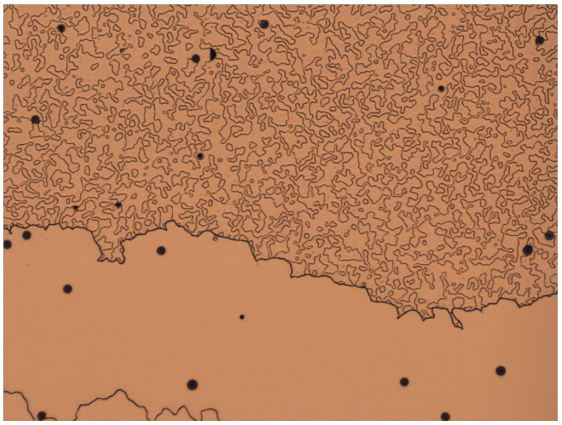

(f) After annealing and synthesis

Figure 15: Different grain structures of copper. All images have 5x magnification. (a) Typical copper surface right after it has been evaporated. (b-f) Different copper films after annealing and graphene synthesis showing different features that appear during them.

was evaporated and the thickness of the films were 600 nm. Perhaps a more important difference was the annealing pressure, which was in their case 5300 Pa (53 mbar), while in this work annealing was done under atmospheric pressure.

It is not clear why there are such differences between the samples in Figure 16. The parameters that were used to fabricate the samples were the same for the most samples and even for the sample in Figure 15f were close to the others. This leaves a few options. For the processing related reasons, either the CVD furnace system does not behave consistently or something during the pre-processing (sapphire cleaning and Cu evaporation) steps causes differences to the samples. Looking at the CVD setup, the possible sources of this type of inconsistencies are in temperature measurement and in gas flow controls. The temperature was measured both by the furnace at the heater coil and by the thermocouple inside a rod that was used to move samples in and out of the furnace. In all processing runs these two measurements were in agreement, so it is very unlikely that the temperature measurement is the reason. It would be more likely that the gas flowmeters would cause the differences, since the flowmeters were old. However, the graphene synthesis should also be affected by the differences in the gas flows, but these kinds of drastic effects were not found. Also, the annealing effect seen here is the result of interactions between the sapphire substrate and the copper film at their interface. This makes it seem implausible that differences in gas flows on the copper/gas interface could cause these differences in the films. Therefore the differences in the CVD parameters could not be the cause of the discrepancies.

This leaves one to suspect that the reason lies either in cleaning of the sapphire or in evaporation. Evaporation is done using extremely pure copper and the parameters between different batches were almost the same. Also the samples that were made during the same evaporation run, for example films in Figures 15b and 15c, show differences, which means that evaporation process can not be the reason for the differences. Sapphire cleaning before evaporation is the only possible processing step remaining. Yet again, the samples in Figure 15 were processed the same way, by cleaning the sapphire substrates using hot acetone and rinsing them with IPA afterwards. A few samples were cleaned using oxygen plasma treatment just before the evaporation, but the samples processed this way still had inconsistent features on them after annealing and growth.

This leads one to think that the different features are not caused by these processes mentioned above, but the sapphire substrate itself. It was observed during processing of different samples that the sapphire substrates that had been used before for graphene synthesis and had the copper etched and cleaned showed a feature on copper from previous run. When copper is evaporated on a sample substrate, the substrate is clamped on a sample stage using metal clamps. Since evaporation is a line-of-sight type technique this leaves a shadow of the clamp, which has only bare sapphire. When the graphene is grown, the copper etched away, the substrate cleaned, copper evaporated again on the same substrate and the sample is placed again in the furnace, the resulting copper film has a feature which corresponds to the clamp shadow of the previous cycle. It is important to note that the feature from the previous run does not appear after the second evaporation, but only after the sample has been in the furnace for the second time. From here we can say that

the sapphire reacts somehow either with the gases or with copper. This would mean that sapphire is reduced by hydrogen or copper diffuses into its crystal lattice. It was not studied further, which of these was the reason for the clamp shadow feature appearing, since studying the problem with the differences in copper grain features was not the point of this study. However, to understand better how to fabricate the copper film, studying this would be important.

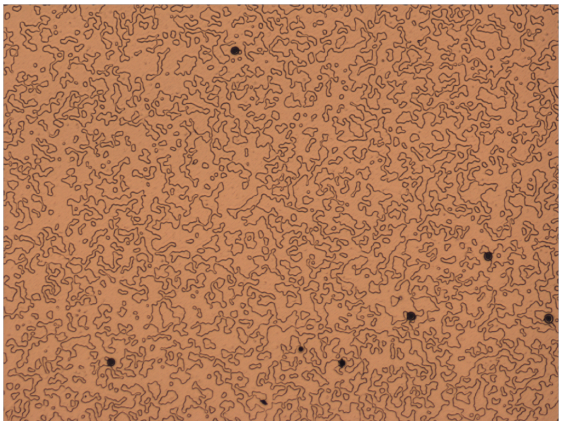

(a) Graphene on Cu, OM image (5x)

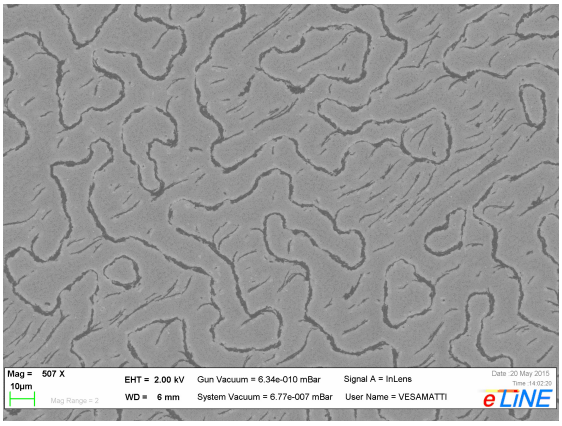

(b) Graphene on Cu, SEM image

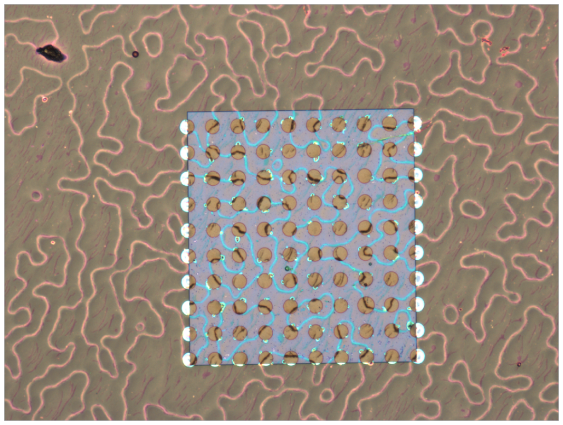

(c) Graphene on membrane with PMMA support, OM image (20x)

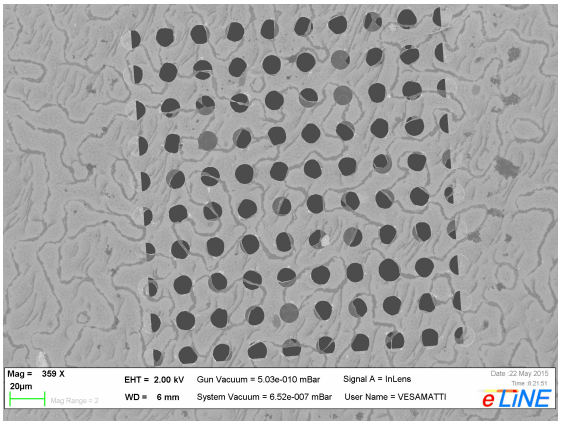

(d) Graphene on membrane, SEM image

Figure 16: OM and SEM images of a graphene sample. (a-b) Graphene on copper after synthesis taken with OM (5x) and SEM respectively. (c) An OM image of graphene on Si_3N_4 membrane before removal of PMMA support layer. (d) SEM image of graphene on Si_3N_4 membrane after PMMA removal.

The effect of grain size and thermal grooves on graphene growth is presented in Figure 16. The images are from the same graphene sample, but not from the exactly same points. Figure 16a has an OM image that is taken after graphene synthesis and Figure 16b is a SEM image of the same graphene sample on copper. Figure 16c is an OM image from the same sample after transfer, but before removing PMMA and Figure 16d an SEM image of the sample after transfer and PMMA removal. Firstly what these images present is that increasing the size of copper grains is important because thermal grooves are places where graphene nucleation is increased, as can

be seen from Figures 16a and 16b. These images present that multilayer graphene domains are far more common in thermal grooves than in the middle of a flat copper grain.

Additionally from Figure 16 it can be seen that these patterns are preserved even when the copper is etched and the graphene is transferred. Looking at these images it is obvious that grooves from grain boundaries in Figures 16a and 16b have the same shape as multilayered grooves in Figures 16c and 16d. In some Si_3N_4 membrane openings the dark lines extend over the opening even tough the thinner sheet has been broken. This observation points to darker lines being more durable than thinner sheets, which is also in line with these darker areas being multilayer areas.

To confirm that darker lines in graphene visible in Figure 16 are multilayered graphene, Raman measurements were performed. SEM images and Raman measurements from a suspended graphene sample are shown in Figure 17. In Figure 17a is a lower magnification SEM image of one suspended graphene sample with two of the openings marked. These openings are the ones that Raman spectra were measured from. In Figure 17b is a SEM image of an intact graphene membrane with circle marks in places where Raman spectra were measured. The spectrum from center of the membrane is in Figure 17c and from the lower part is in 17d. In Figure 17e is a SEM image of one of the strands that stretches over an opening while the rest of the membrane has been broken. A Raman spectrum from this "bridge" is presented in Figure 17f.

In Figure 17b is an image of a graphene membrane that has lines that are more lightly colored than rest of the membrane material. These lines appear dark on nitride film while rest of the graphene film is lighter. A Raman spectrum taken from the middle of the membrane in Figure 17c shows that 2D/G ratio of graphene in this spot is 0.80, giving that graphene in this spot does have more than one layer [82, 83]. A Raman spectrum in Figure 17d taken from outside of the line has 1.40 2D/G intensity ratio, which points to single layer graphene. These results are clear evidence that graphene form multilayer structure in copper thermal grooves, since the lines come directly from the structure that copper forms during annealing. An interesting result is that in spectrum 17c, the D band is actually the most intense of all the bands. This indicates that graphene at these lines is very defective, since the D band intensity is significantly lower in Figure 17d. These lines are also quite narrow, about 1 μm wide, meaning that piled up graphene domains necessarily have lots of edges which contribute to D band. This points to extra stacked layers over graphene being very small crystals. Figure 17f has a Raman spectrum from the graphene bridge in Figure 17e with 2D/G ratio of 0.55. This also shows that these lines are multilayered graphene.

Another observation that back this is that Raman peaks shift between single layer in 17d and multilayer in 17f. In 17d the G band is at 1600 cm^{-1} and the 2D band at 2672 cm^{-1}, while in 17f the G band is at 1590 cm^{-1} and 2D at 2682 cm^{-1}. Shifts of the G band to lower wavenumber and the 2D band to higher is observed to happen as more layers of graphene are stacked [80]. In 17c peak positions are about the same as in 17d and come within the accuracy of the spectrometer. This can be explained by a lower amount of stacked layers in 17c than in 17f, which can also be seen from higher 2D/G ratio, and therefore there is less shift in peak positions. Also in a TEM

image in Figure A5 these lines can be seen, but the multilayer areas do not appear to be very thick. An image with higher magnification in Figure A6 also shows that the lines are not very thick or wide.

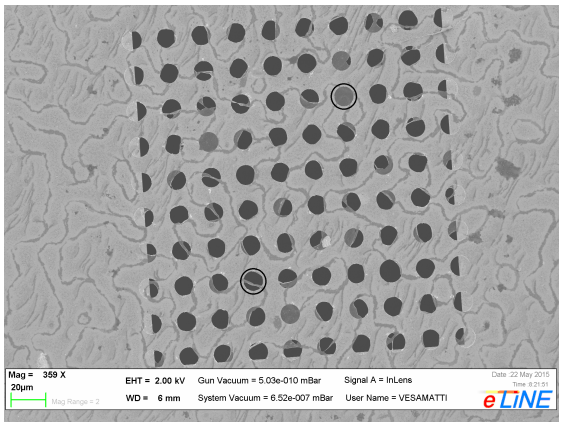

(a) Overview

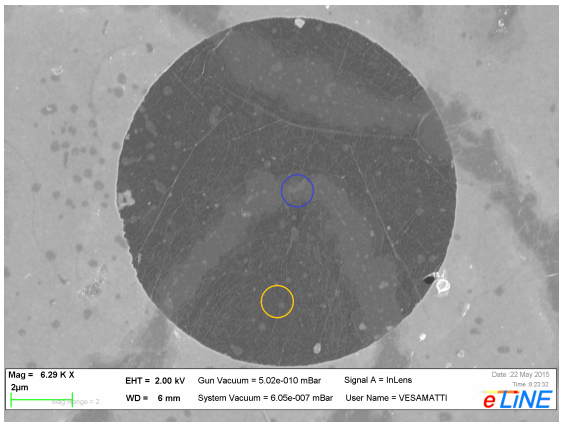

(b) Graphene membrane

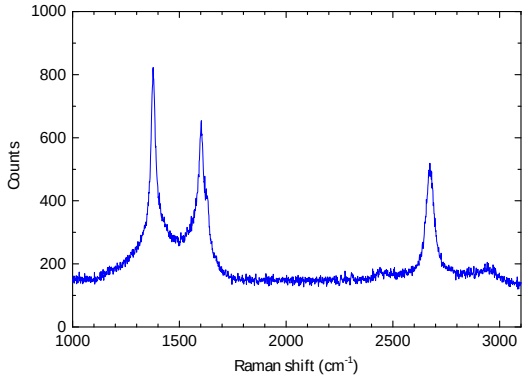

(c) Raman spectrum from center

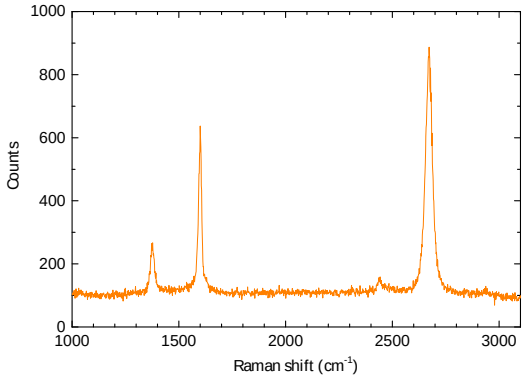

(d) Raman spectrum from lower marker

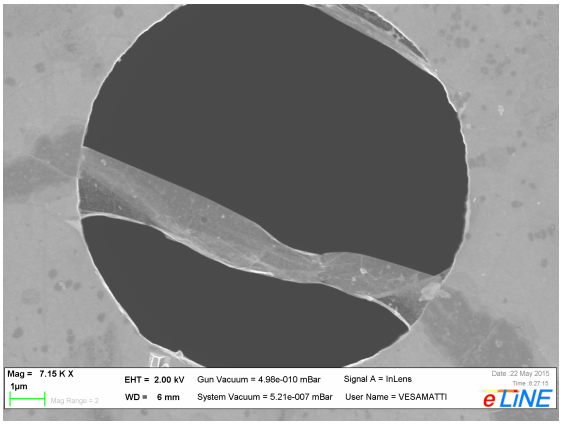

(e) Graphene bridge

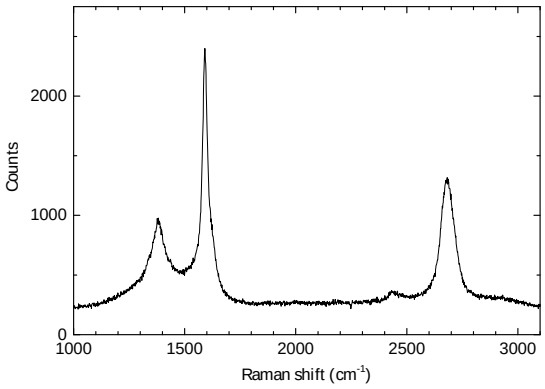

(f) Raman spectrum from the bridge

Figure 17: SEM images and Raman measurements of suspended graphene sample. (a) An overview of the sample with circles around the suspended graphene membranes that were studied further. (b) A closeup SEM image of a graphene membrane with markers where Raman spectra were measured. (c) A spectrum taken at the center of the graphene membrane in b. (d) A spectrum from the lower part in b. (e) A closeup SEM image of a graphene bridge. (f) A Raman spectrum from the bridge in e.

4.2 Amorphous carbon contamination

A problem early on during the experimental work was that the quality of graphene was very poor, meaning that the synthesized carbon films did not have single graphene layer, but multilayers and even amorphous carbon instead of graphene. At this point the assumed reason for why there were so much multilayer graphene instead of monolayer graphene was that the concentration of carbon precursor during the CVD synthesis was too high, since in many articles the carbon concentration is very low [86, 87, 88].

Only decreasing the carbon flow into the furnace did not however improve results. The improvement only arise when comparing two samples from the same growth, but at different position in the quartz sample holder tube. When comparing these, the sample which was at exhaust side of furnace had some areas with even monolayer graphene, even tough most of the area still was covered with graphite-like carbon. Following growths confirmed that moving the copper/sapphire substrates farther from the leading end of the tube improved the results. Some samples show a transition from amorphous carbon to graphene.

Images and Raman measurements from this kind of sample is presented in Figure 18. Figure 18a shows a low magnification (5x) image of a sample that has been transferred onto SiO_2 and annealed for two hours at 300 °C under oxygen atmosphere to remove graphitic carbon and make graphene areas visible. These spots can clearly be seen and their number and size increases from bottom to top of the image, which was also the direction of flow during growth. On the upper left part of the image these spots form a continuous film, whereas on the lower part these spots are completely absent. An SEM image of this same sample before annealing in Figure 18b is showing that inside of the spots there are different domains that look like graphene with different number of layers and graphene has also folded in some places. Outside of the spots there is only a homogenous looking surface. In Figure 18b there are also markers where Raman spectra have been measured. These spectra are presented in Figures 18c and 18d. The broad peaks in both spectra at 1000 cm^{-1} are from silicon. The surface outside of the spots can not be called graphene, but rather amorphous carbon with broad and partly fused peaks at 1345 cm^{-1} and 1561 cm^{-1} and also a very broad and low intensity peak around 2825 cm^{-1}. Inside these spots there are the three expected carbon peaks, D at 1377 cm^{-1}, G at 1591 cm^{-1} and 2D at 2677 cm^{-1}, with 2D/G intensity ratio of 1.2, indicating single layer graphene.

Annealing removed the amorphous type of carbon, but left graphene spots, which was expected since these amorphous carbon films were highly disordered and therefore more susceptible to chemical reactions than graphene. As mentioned above, only decreasing the precursor flow into the furnace did not cause significant improvement without moving the samples further into the sample holder tube. This is however related to decreasing carbon concentration at the sample, since the quartz tube walls get carbon deposition, which becomes visible after three to five runs. Since carbon deposits on the walls it reduces the carbon concentration at the sample if it is pushed well inside the tube.

Figure 19 has more SEM images of the amorphous carbon film. Figure 19a shows graphene and amorphous carbon domains on same sample after synthesis on Cu. An image with lower magnification showing the majority of the sample can be seen in

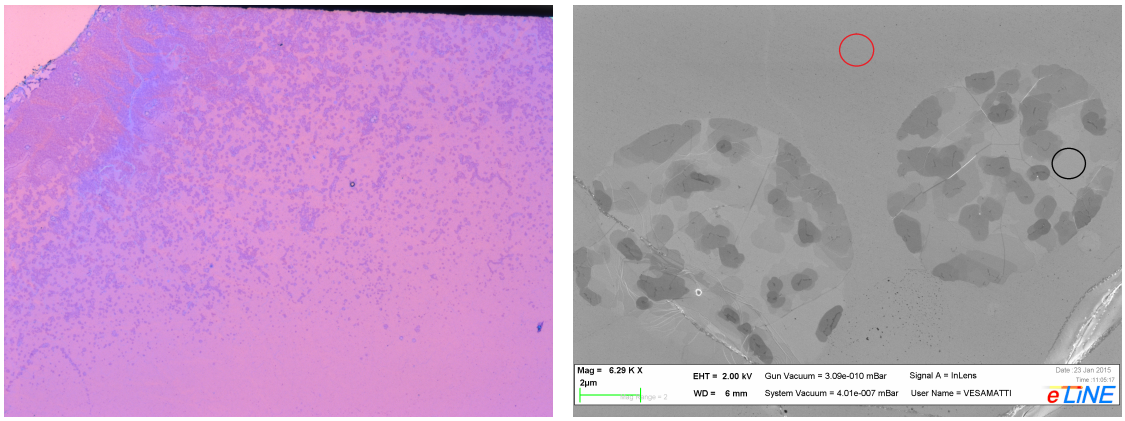

(a) OM image

(b) SEM image

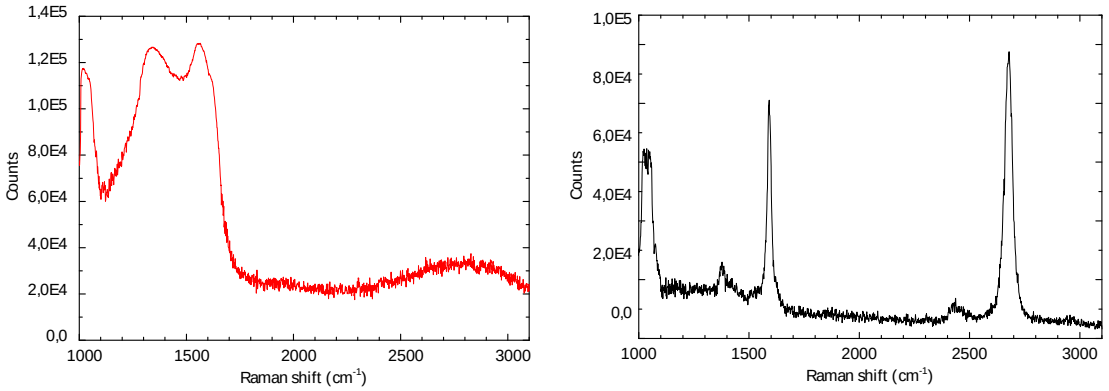

(c) Red spot

(d) Black spot

Figure 18: (a) An OM image of graphene transferred onto SiO_2 with 5x magnification. (b) A SEM image of the same sample. (c) A Raman spectrum from red spot in b. (d) A Raman spectrum from black spot in b.

Figure A1, where it can be seen that the sample is roughly divided into two areas, amorphous and graphene, and in-between there is a mix of these. In Figure 19b is an image with higher magnification, where it can be seen that areas with lighter color are graphene with some multilayers and darker areas with amorphous carbon. There seems to be a boundary layer in-between these where the carbon is not amorphous, but most likely multilayer graphene. This boundary layer is shown more closely in Figure 19c, while in 19d shows some amorphous carbon islands in an area which has only graphene for the most part. Unlike graphene within amorphous carbon film these spots are not necessarily circular in shape. Figure 19e displays one of the graphene circles after transferring it to Si_3N_4 membrane and annealing in O_2. This shows clearly circular graphene spots that have been left while amorphous carbon has been etched away. Figure 19f is taken at a different location of the same sample and shows two partially suspended graphene circles and a hole in between them. Graphene in areas without amorphous carbon is quite good, although the amount of multilayer domains is large. High magnification images of graphene on copper and suspended can be seen in Figures A3 and A4.

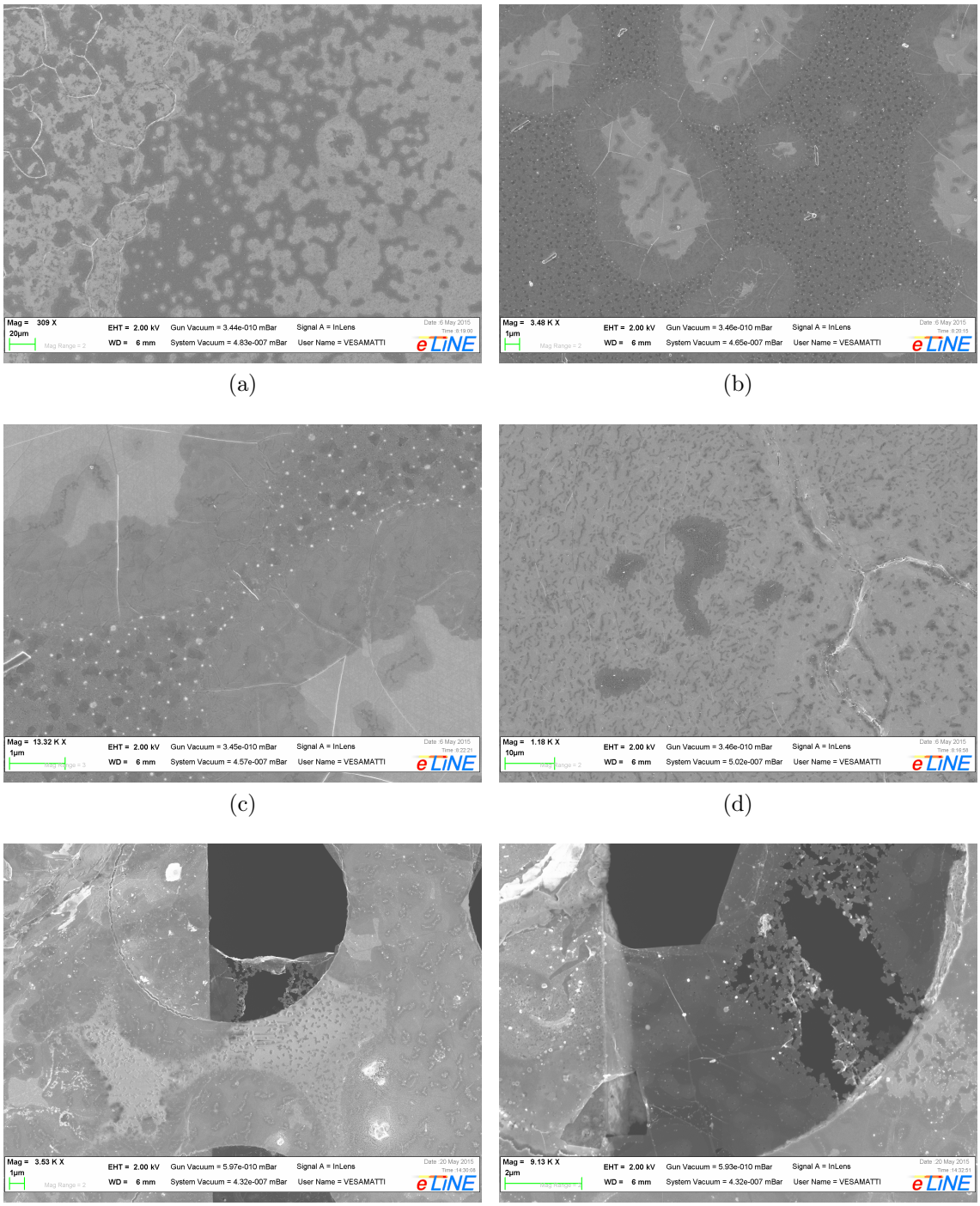

Figure 19: SEM images of amorphous carbon mixed with graphene. (a) Graphene islands (light) within area of amorphous carbon (dark). (b) An image of graphene islands with higher magnification. (c) Boundary between graphene and amorphous carbon. (d) Amorphous carbon islands within graphene. (e) Same sample after transferring graphene onto Si_3N_4 membranes. (f) A higher magnification image of a suspended graphene circle.

According to the results in Figure 18, amorphous carbon forms where carbon concentration is high. The spread of amorphous carbon for some reason seems to "avoid" some areas which leaves graphene circles within amorphous carbon. Some of these spots have an impurity particle in the middle of the circle, which might somehow shield graphene, but not all of the circles have these, such as a circle in appendix Figure A2. However it is possible that the particles have been moved after sample was taken from 1000 °C furnace. Between these two extremes seems to be multilayer graphene, since folding (white lines in 19b and 19c) in graphene continues to this intermediate layer but stops at regions with amorphous carbon. Annealing in oxygen completely removes amorphous carbon and interestingly leaves graphene between circles shredded as can be seem from Figures 19e and 19f. The fact that narrow graphene strands hold quite large pieces of graphene from falling even under electron beam irradiation demonstrates the strength of graphene.

4.3 Optimization of growth parameters

One of the most important graphene synthesis parameters is the gas flow and especially carbon content in the flow. Figure 20 has images and Raman spectra that demonstrate the effect of carbon concentration to graphene synthesis. In Figure 20a is a SEM image and in Figure 20b a Raman spectrum of graphene synthesized and transferred onto a silicon nitride membrane window. This sample was synthesized during 20 minutes, using 65 sccm Ar + H_2 (6% H_2) flow to bubbler and 40 sccm pure Ar to dilute the gas mixture. In Figures 20c and 20d is a sample that was synthesized using 100 sccm Ar and 30 sccm H_2 as bubbler flow and 470 sccm pure Ar for dilution. The growth time was 15 minutes. A similar sample in Figures 20e and 20f was fabricated with 50 sccm Ar and 20 sccm H_2 as bubbler flow and 530 sccm Ar for dilution, with a growth time of 5 minutes. Another sample that can be taken into consideration is in Figure 17, which was synthesized with 20 sccm Ar and 20 sccm H_2 as bubbler flow and 560 sccm Ar dilution, using a growth time of 5 minutes. The reason for widely varying numbers of counts in Raman spectra in Figure 20 is because of different acquisition times.

Results in Figure 20 clearly demonstrate the higher quality of graphene when carbon concentration is lowered. The sample in Figures 20a and 20b is multilayered and defective, but it is not amorphous, like in Figure 18. In Figures 20c and 20d the graphene is a few layers thick and in Figures 20e and 20f it is a single layer. These spectra are taken from one spot only, so they do not represent the complete sample, but differences within the samples can be seen quite well from SEM images. The first sample in Figure 20a is the most homogenous in film quality. There are not much variations in SEM image and also Raman spectra that were measured from different points on the sample are very similar. The sample in Figure 20c has more variations. There are many impurities and some folding with darker regions in the suspended area, which are single layer graphene, see spectrum in appendix Figure A7. Impurities and edges between single and multi layered graphene can also be seen from Figure A8 in appendix. A sample in Figure 20e is mostly single layered, but also in this sample there are impurities and folding in addition to some holes in the graphene membrane.

When these samples are compared, it is clear that lowering carbon concentration

in gas flow improves the quality of graphene. It is obvious that the first sample in Figure 20 was fabricated with too high carbon concentration. The concentration was much better in other samples, but they have clear differences also. Even tough the two lower samples in Figure 20 both have single layer areas and multilayer areas, in the middle sample multilayer areas are clearly more common than single layered areas. There are also much more holes in the graphene membranes, which also points to graphene being thinner and therefore easier to break. When comparing the sample in Figures 20e and 20f to sample in Figure 17 the quality is not much different. Both have many layered and single layered graphene, but sample in Figure 17 has multilayer areas "collected" into lines whereas with sample in 20e the sample has small multilayer domains randomly scattered on the film. Outside of the multilayer lines the graphene does seem to be slightly better than in sample in 20e, meaning that there is a bit less multilayer domains.

Other parameters beside carbon concentration in gas flow were not studied. A choice was made to prioritize the study of carbon concentration since that was the parameter that had the most effect in graphene quality. Still some parameters were changed a bit in order to improve the growth. Growth time is the time that the catalyst surface is exposed to precursor so it is tied to carbon concentration. Growth time was decreased in latter growths and it is partly responsible also for changes in the samples presented in 20. The growth time was decreased to 5 minutes and was not changed in subsequent synthesis runs, because that time allowed full graphene coverage and still made it possible to synthesize single layers. The temperature was kept at 1000 °C for most of the growths. Four samples in two different runs were synthesized using 1060 °C, but there were no noticeable difference in graphene quality. Using low pressure was not possible for the current CVD setup, so the effect of pressure to the synthesis was not studied.

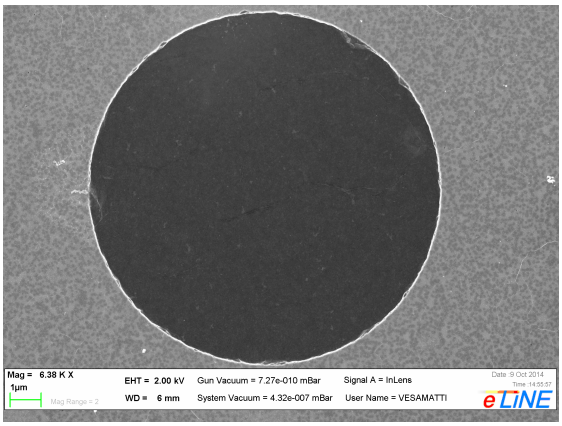

(a)

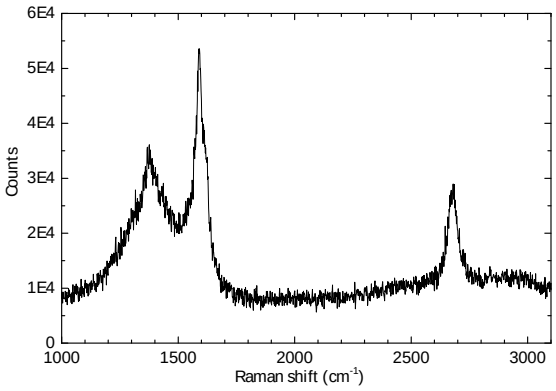

(b)

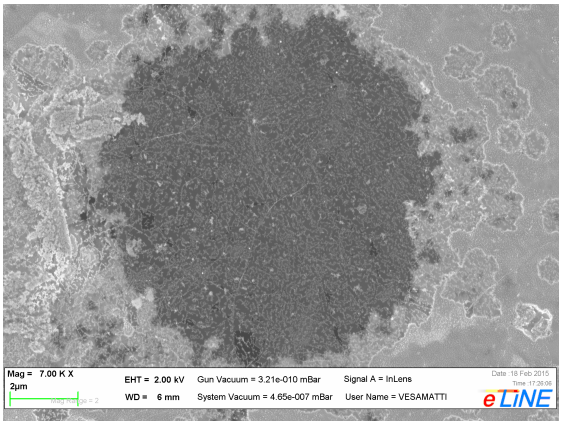

(c)

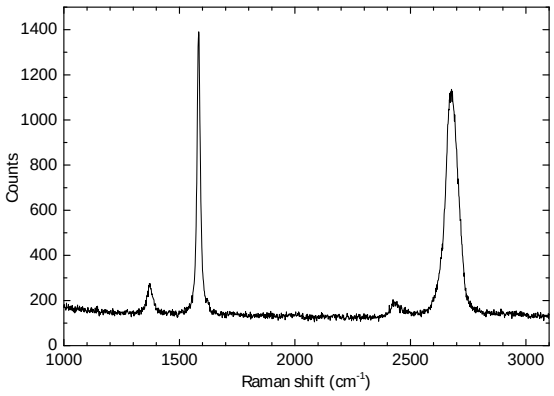

(d)

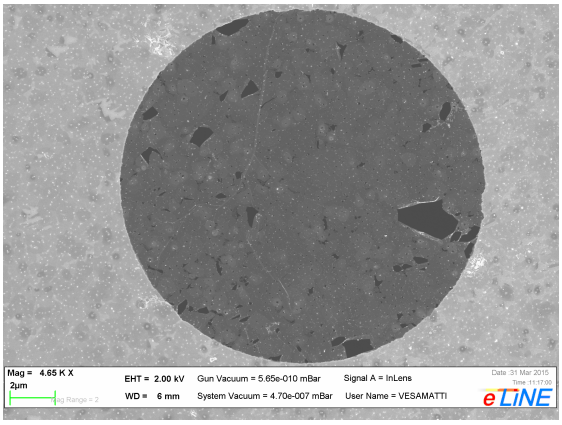

(e)

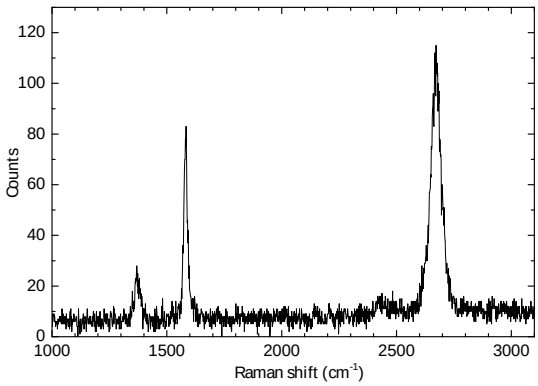

(f)

Figure 20: SEM images and Raman spectra from graphene samples synthesized with different growth parameters. (a-b) 65 sccm Ar + H_2 + 40 sccm Ar, 20 min. (c-d) 100 sccm Ar + 30 sccm H_2 + 470 sccm Ar, 15 min. (e-f) 20 sccm Ar 20 sccm H_2 + 560 sccm Ar, 5 min.

4.4 PMMA removal from suspended graphene

Graphene transfer onto a Si_3N_4 membrane with open windows patterned into it is a bit more tricky than transfer onto a flat substrate. To study which PMMA removal method is the best for suspended graphene a few different processes were tried, such as annealing with different temperatures and gases and critical point drying.

Examples of samples processed with these different methods are shown in Figure 21. In Figure 21a is a sample where PMMA was removed by annealing at 300 °C under O_2 atmosphere. An example of a sample where PMMA is removed using CPD is in Figure 21b. First of all these images show that the transfer processes do work. Both of the samples have the majority of the openings covered with intact graphene. Differences in these samples are that the sample made using CPD seems to have more impurities. Clearly O_2 is more effective in cleaning PMMA and other residues than only immersing the sample into acetone. This was an expected result since PMMA is a hydrocarbon, so it readily reacts with oxygen. Perhaps a more surprising result was that graphene survived the annealing as well as it did. These graphene samples were clearly multilayered, which was confirmed with Raman spectroscopy. Raman spectra measured from these samples are in appendix, Figures A9 and A10. A sample that is fabricated with CPD can be annealed to clean it from impurities and residues, but if only annealing works just the same of even better there is no reason to use CPD. Therefore at an early point of this work annealing was the preferred method for removing PMMA layer after transfer.

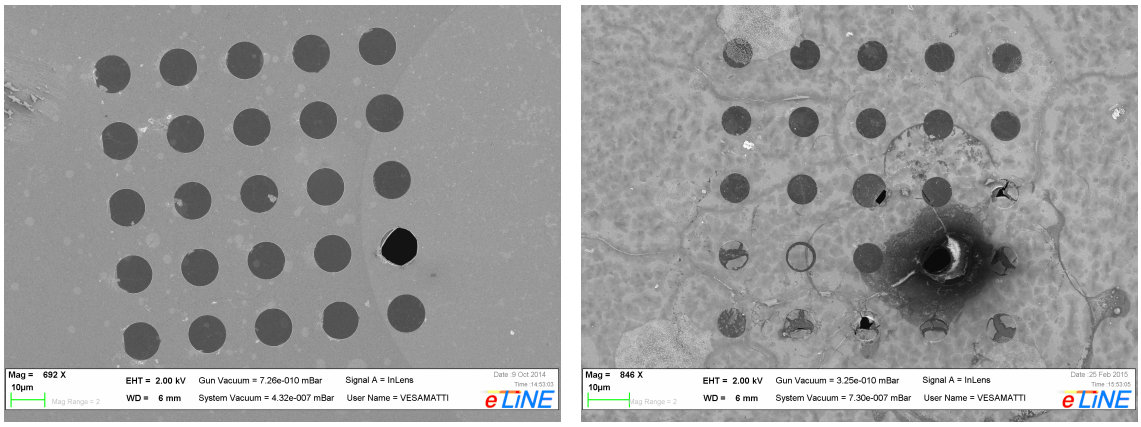

(a) Annealing (b) CPD

Figure 21: SEM images of two samples after transfer and PMMA removed using (a) annealing at 300 °C in O_2 and (b) critical point drying.

Both of the methods to remove PMMA worked with samples that had many layers of graphene, but as the synthesis was improved also differences in PMMA removing appeared. In Figure 22 SEM images of mostly monolayer graphene are presented. In Figure 22a the sample was annealed again at 300 °C in oxygen atmosphere and in Figure 22b the sample was prepared using CPD. These samples have only some multilayer domains besides single layer graphene, which was confirmed with Raman spectroscopy. Spectra of these samples are in appendix Figures A11 and A12. These images demonstrate that in this case after annealing all but two of the suspended

graphene membranes were broken, while with CPD there are much more graphene still left, even tough many of them seem to have small holes. Also, like before, those graphene membranes that are still left after annealing are much cleaner compared to the sample cleaned with CPD. With single layer samples the problem of graphene membranes breaking was consistent with different samples. An example of a sample where all suspended graphene membranes were destroyed is in Figure A13. Even tough graphene suspended over openings was destroyed, graphene on nitride was still present, meaning that graphene was not burnt. This was verified by annealing a graphene sample with PMMA in nitrogen atmosphere, where the graphene membranes did not survive even tough PMMA was not even completely removed after 3 hour annealing at 300 °C. An explanation to this problem is that, when samples are heated to annealing temperature, they cross over the melting temperature of PMMA. It is likely that while multilayer graphene is strong enough to hold the PMMA, the single layer graphene membrane does not have enough strength to support polymer that has lost its rigidity, even when the thickness of the PMMA layer is only about hundred nanometers.

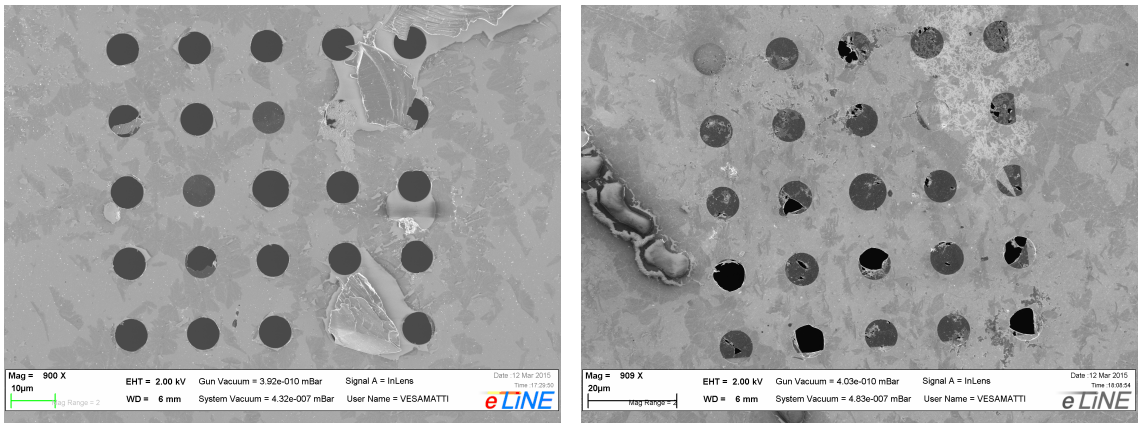

(a) Annealing (b) CPD

Figure 22: SEM images of two single layer graphene samples after transfer and PMMA removed using (a) annealing at 300 °C in O_2 and (b) critical point drying.

The next step was to study how annealing affects suspended graphene that has been processed using CPD. In Figure 23 are images of this kind of sample before and after annealing in oxygen at 300 °C for one hour. When comparing 23a and 23b it can be seen that many of the impurities have been removed during annealing. On the other hand in some graphene membranes sizes of holes have increased. When comparing images of a membrane in the middle in Figures 23c and 23d it is clear that the sample has become cleaner during annealing. In the image after annealing some matter has been removed that was covering graphene in 23c. In the image after annealing, areas with different number of layers are visible, while in the image before annealing all of the graphene seems to have the same thickness because of all residues attached on the graphene. However, O_2 annealing at 300 °C does not seem to be enough to clean even nearly all of the impurities, but still this is a step to the right direction. This particular sample had plenty of impurities on it, but annealing works well also on samples that are much cleaner to begin with. An example of this

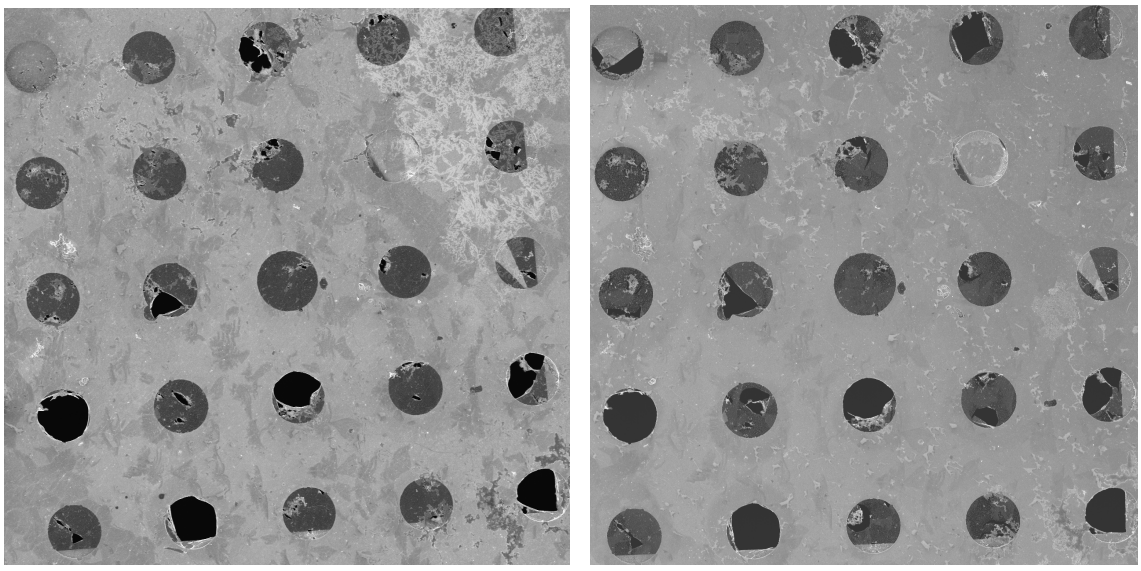

(a) Before (b) After

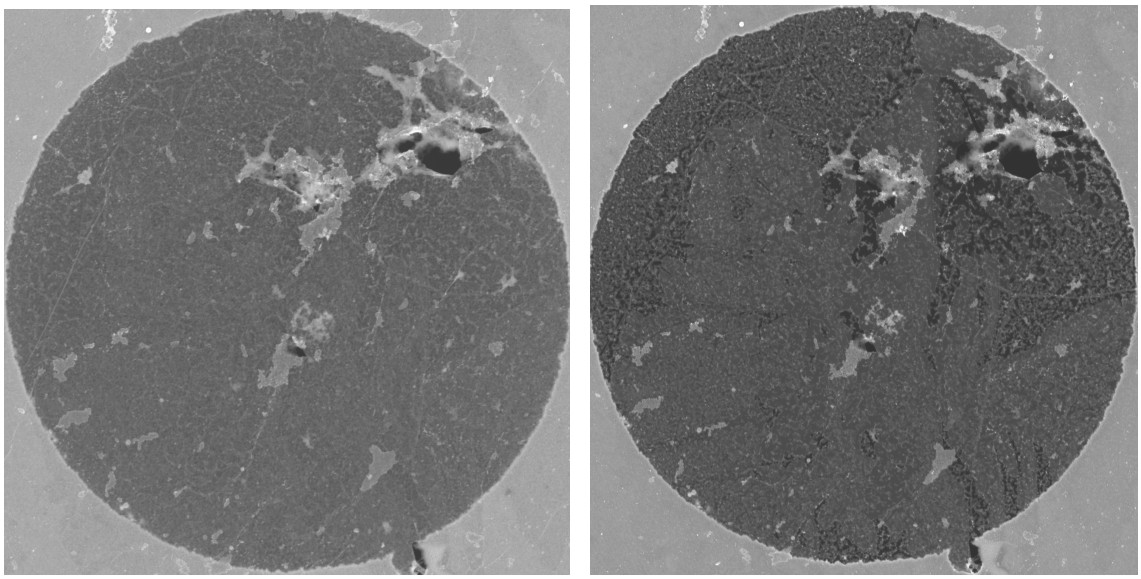

(c) Before (d) After

Figure 23: SEM images of a suspended graphene sample showing the whole area (a) before and (b) after annealing and an opening in the center (c) before and (d) after annealing.

is shown in Figure A14, where a sample that does not have much impurities clearly becomes more clean with annealing. Annealing was also studied using nitrogen as annealing gas instead of oxygen. Results of these experiments in Figure A15 show that the same effect is present also when using nitrogen. A more thorough study of which annealing gases, temperatures, times etc. are optimal for graphene cleaning would be very beneficial, but it is beyond the scope of this work.

5 Conclusions

Overall the work done here was successful. Silicon nitride membranes with openings were fabricated and graphene was synthesized and transferred onto them to create suspended graphene devices. However there are still many things that can be done.

One of the aspects of this work that should be studied further is how to make the copper catalyst surface so that there is as little as possible grain boundaries, which cause multilayer graphene growth. One option is to use a heated deposition stage as copper is deposited, as was done in [53]. Results acquired in this work were not consistent in the sense that there were many different grain sizes and thermal groove shapes even tough the samples were treated the same way. Improving copper grain sizes can also increase the quality of graphene, so it would be important to improve consistency of copper films.

During this work there was a problem with forming of amorphous carbon, which is connected to carbon concentration in vicinity of copper surface. This was solved by moving samples farther into the quartz sample holder tube, which caused decreased carbon concentration since carbon adsorbs on the quartz walls. Decreasing carbon flow further is one thing that can be done. Even in the best samples there were some multilayer domains, which can be tried to decrease by reducing amount of carbon. This is however quite difficult with the current setup, which uses ethanol as precursor, since the amount of carbon can not be controlled well. To improve the situation a possibility is to change to gaseous precursor, such as methane. This would make it much easier and reliable to control carbon flow and additionally this also enables the use of low pressure during synthesis.

Pressure is only one of the parameters that has an effect on the graphene synthesis. To improve the quality of graphene one should also study the effect of other parameters, such as temperature, growth time, hydrogen concentration, pulsing of precursor etc. The mapping of parameter space, although laborious, is the only way to find the optimum conditions for graphene synthesis.

Finding a good transfer process in which graphene can be suspended without damaging it was one of the most important parts of this project. The removal of PMMA with CPD was found to be the working method for single layer graphene, but it leaves residues which need to be cleaned. The most promising cleaning method is thermal annealing, which was studied a bit in this work, but it can be studied further to find out the best method to clean graphene without damaging or doping it. Another possible improvement to the process could be the use of different support polymer layer instead of PMMA. These could be for example polystyrene or polycarbonate which would leave less residues on graphene than PMMA.

Suspended graphene made this way can be used in further research. One possible way to utilize the samples could be to make suspended electrical devices. This is very difficult to do with current equipment in the Nanoscience Center, but with the upcoming Helium Ion Microscope these devices can be done.

References

[1] K. S. Novoselov, A. K. Geim, S. V. Morozov, D. Jiang, Y. Zhang, S. V. Dubonos, I. V. Grigorieva, and A. A. Firsov. Electric Field Effect in Atomically Thin Carbon Films. *Science*, 306:666–669, 2004.

[2] P. R. Wallace. The Band Theory of Graphite. *Physical Review*, 71:622–634, 1947.

[3] A. K. Geim and K. S. Novoselov. The rise of graphene. *Nature materials*, 6:183–191, 2007.

[4] K. S. Novoselov, D. Jiang, F. Schedin, T. J. Booth, V. V. Khotkevich, S. V. Morozov, and A. K. Geim. Two-dimensional atomic crystals. *Proceedings of the National Academy of Sciences of the United States of America*, 102(30):10451–10453, 2005.

[5] E. Pop, V. Varshney, and A. K. Roy. Thermal properties of graphene: Fundamentals and applications. *MRS Bulletin*, 37:1273–1281, 12 2012.

[6] C. Lee, X. Wei, J. W. Kysar, and J. Hone. Measurement of the Elastic Properties and Intrinsic Strength of Monolayer Graphene. *Science*, 321:385–388, 2008.

[7] R. R. Nair, P. Blake, A. N. Grigorenko, K. S. Novoselov, T. J. Booth, T. Stauber, N. M. R. Peres, and A. K. Geim. Fine Structure Constant Defines Visual Transparency of Graphene. *Science*, 320, 2008.

[8] X. Miao, S. Tongay, M. K. Petterson, K. Berke, A. G. Rinzler, B. R. Appleton, and A. F. Hebard. High Efficiency Graphene Solar Cells by Chemical Doping. *Nano Letters*, 12(6):2745–2750, 2012.

[9] C. Liu, Z. Yu, D. Neff, A. Zhamu, and B. Z. Jang. Graphene-Based Supercapacitor with an Ultrahigh Energy Density. *Nano Letters*, 10(12):4863–4868, 2010.

[10] Ermete Antolini. Graphene as a new carbon support for low-temperature fuel cell catalysts. *Applied Catalysis B: Environmental*, 123-124:52 – 68, 2012.

[11] L. Wu, H. S. Chu, W. S. Koh, and E. P. Li. Highly sensitive graphene biosensors based on surface plasmon resonance. *Opt. Express*, 18(14):14395–14400, 2010.

[12] H. Tian, Y. Shu, X.-F. Wang, M. A. Mohammad, Z. Bie, Q.-Y. Xie, C. Li, W.-T. Mi, Y. Yang, and T.-L. Ren. A Graphene-Based Resistive Pressure Sensor with Record-High Sensitivity in a Wide Pressure Range. *Scientific Reports*, 5(8603), 2015.

[13] H. J. Yoon, D. H. Jun, J. H. Yang, Z. Zhou, S. S. Yang, and M. M.-C. Cheng. Carbon dioxide gas sensor using a graphene sheet. *Sensors and Actuators B: Chemical*, 157(1):310 – 313, 2011.

[14] M. G. Chung, D. H. Kim, H. M. Lee, T. Kim, J. H. Choi, D. K. Seo, J.-B. Yoo, S.-H. Hong, T. J. Kang, and Y. H. Kim. Highly sensitive NO2 gas sensor based on ozone treated graphene. *Sensors and Actuators B: Chemical*, 166-167:172 – 176, 2012.

[15] M. G. Chung, D. H. Kim, D. K. Seo, T. Kim, H. U. Im, H. M. Lee, J.-B. Yoo, S.-H. Hong, T. J. Kang, and Y. H. Kim. Flexible hydrogen sensors using graphene with palladium nanoparticle decoration. *Sensors and Actuators B: Chemical*, 169:387 – 392, 2012.

[16] M. C. Lemme, T. J. Echtermeyer, M. Baus, and H. Kurz. A Graphene Field-Effect Device. *Electron Device Letters, IEEE*, 28(4):282–284, 2007.

[17] L. Vicarelli, M. S. Vitiello, D. Coquillat, A. Lombardo, A. C. Ferrari, W. Knap, M. Polini, V. Pellegrini, and A. Tredicucci. Graphene field-effect transistors as room-temperature terahertz detectors. *Nature Materials*, 11(10):865–871, 2012.

[18] X. Cai, A. B. Sushkov, R. J. Suess, M. M. Jadidi, G. S. Jenkins, L. O. Nyakiti, R. L. Myers-Ward, S. Li, J. Yan, D. K. Gaskill, T. E. Murphy, H. D. Drew, and M. S. Fuhrer. Sensitive room-temperature terahertz detection via the photothermoelectric effect in graphene. *Nature Nanotechnology*, 9(10):814–819, 2014.

[19] H. Yan, X. Li, B. Chandra, G. Tulevski, Y. Wu, M. Freitag, W. Zhu, P. Avouris, and F. Xia. Tunable infrared plasmonic devices using graphene/insulator stacks. *Nature Nanotechnology*, 7(5):330–334, 2012.

[20] D. R. Cooper, B. D'Anjou, N. Ghattamaneni, B. Harack, M. Hilke, A. Horth, N. Majlis, M. Massicotte, L. Vandsburger, E. Whiteway, and V. Yu. Experimental Review of Graphene. *ISRN Condensed Matter Physics*, 2012:1–56, 2012.

[21] K. V. Emtsev, A. Bostwick, K. Horn, J. Jobst, G. L. Kellogg, L. Ley, J. L. McChesney, T. Ohta, S. A. Reshanov, J. Röhrl, E. Rotenberg, A. K. Schmid, D. Waldmann, H. B.Weber, and T. Seyller. Towards wafer-size graphene layers by atmospheric pressure graphitization of silicon carbide. *Nature materials*, 8:203–207, 2009.

[22] S. Stankovich, D. A. Dikin, R. D. Piner, K. A. Kohlhaas, A. Kleinhammes, Y. Jia, Y. Wu, S. T. Nguyen, and R. S. Ruoff. Synthesis of graphene-based nanosheets via chemical reduction of exfoliated graphite oxide. *Carbon*, 45(7):1558 – 1565, 2007.

[23] L. Jiao, L. Zhang, X. Wang, G. Diankov, and H. Dai. Narrow graphene nanoribbons from carbon nanotubes. *Nature*, 458:877–580, 2009.

[24] J.-H. Chen, C. Jang, S. Xiao, M. Ishigami, and M. S. Fuhrer. Intrinsic and extrinsic performance limits of graphene devices on SiO_2. *Nature nanotechnology*, 3(4):206–209, 2008.

[25] X. Du, I. Skachko, A. Barker, and E. Y. Andrei. Approaching ballistic transport in suspended graphene. *Nature nanotechnology*, 3(8):491–495, 2008.

[26] J. C. Meyer, A. K. Geim, M. I. Katsnelson, K. S. Novoselov, T. J. Booth, and S. Roth. The structure of suspended graphene sheets. *Nature*, 446:60–63, 2007.

[27] M. I. Katsnelson. Graphene: carbon in two dimensions. *Materials Today*, 10(1-2), 2007.

[28] Phaedon Avouris. Graphene: Electronic and Photonic Properties and Devices. *Nano Letters*, 10(11):4285–4294, 2010.

[29] T. Shen, W. Wu, Q. Yu, C. A. Richter, R. Elmquist, D. Newell, and Y. P. Chen. Quantum Hall effect on centimeter scale chemical vapor deposited graphene films. *Applied Physics Letters*, 99, 2011.

[30] Y.-C. Chen, T. Cao, C. Chen, Z. Pedramrazi, D. Haberer, D. G. de Oteyza, F. R. Fischer, S. G. Louie, and M. F. Crommie. Molecular bandgap engineering of bottom-up synthesized graphene nanoribbon heterojunctions. *Nature Nanotechnology*, 10(2):156 – 160, 2015.

[31] C.-K. Chang, S. Kataria, C.-C. Kuo, A. Ganguly, B.-Y. Wang, J.-Y. Hwang, K.-J. Huang, W.-H. Yang, S.-B. Wang, C.-H. Chuang, M. Chen, C.-I. Huang, W.-F. Pong, K.-J. Song, S.-J. Chang, J.-H. Guo, Y. Tai, M. Tsujimoto, S. Isoda, C.-W. Chen, L.-C. Chen, and K.-H. Chen. Band Gap Engineering of Chemical Vapor Deposited Graphene by in Situ BN Doping. *ACS Nano*, 7(2):1333–1341, 2013.

[32] J. Aumanen, A. Johansson, J. Koivistoinen, P. Myllyperkiö, and M. Pettersson. Patterning and tuning of electrical and optical properties of graphene by laser induced two-photon oxidation. *Nanoscale*, 7:2851–2855, 2015.

[33] C. Lee, X. Wei, J. W. Kysar, and J. Hone. Measurement of the Elastic Properties and Intrinsic Strength of Monolayer Graphene. *Science*, 321(5887):385–388, 2008.

[34] E. Y Andrei, G. Li, and X. Du. Electronic properties of graphene: a perspective from scanning tunneling microscopy and magnetotransport. *Reports on Progress in Physics*, 75, 2012.

[35] J. S. Bunch, S. S. Verbridge, J. S. Alden, A. M. van der Zande, J. M. Parpia, H. G. Craighead, and P. L. McEuen. Impermeable Atomic Membranes from Graphene Sheets. *Nano Letters*, 8(8):2458–2462, 2008.

[36] S. Franssila. *Introduction to Microfabrication.* John Wiley & Sons Ltd, 2004.

[37] R. Muñoz and C. Gómez-Aleixandre. Review of CVD Synthesis of Graphene. *Chemical Vapor Deposition*, 19(10-11-12):297–322, 2013.

[38] X. Li, W. Cai, J. An, S. Kim, J. Nah, D. Yang, R. Piner, A. Velamakanni, I. Jung, E. Tutuc, S. K. Banerjee, L. Colombo, and R. S. Ruoff. Large-Area Synthesis of High-Quality and Uniform Graphene Films on Copper Foils. *Science*, 324(5932):1312–1314, 2009.

[39] X. Liu, L. Fu, N. Liu, T. Gao, Y. Zhang, L. Liao, and Z. Liu. Segregation Growth of Graphene on Cu-Ni alloy for Precise Layer Control. *The Journal of Physical Chemistry C*, 115(24):11976–11982, 2011.

[40] R. S. Weatherup, B. C. Bayer, R. Blume, C. Ducati, C. Baehtz, R. Schlögl, and S. Hofmann. In Situ Characterization of Alloy Catalysts for Low-Temperature Graphene Growth. *Nano Letters*, 11(10):4154–4160, 2011. PMID: 21905732.

[41] M. H. Rümmeli, A. Bachmatiuk, A. Scott, F. Börrnert, J. H. Warner, V. Hoffman, J. H. Lin, G. Cuniberti, and B. Büchner. Direct Low-Temperature Nanographene CVD Synthesis over a Dielectric Insulator. *ACS Nano*, 4(7):4206–4210, 2010.

[42] X. Ding, G. Ding, X. Xie, F. Huang, and M. Jiang. Direct growth of few layer graphene on hexagonal boron nitride by chemical vapor deposition. *Carbon*, 49(7):2522 – 2525, 2011.

[43] A. Guermoune, T. Chari, F. Popescu, S. S. Sabri, J. Guillemette, H. S. Skulason, T. Szkopek, and M. Siaj. Chemical vapor deposition synthesis of graphene on copper with methanol, ethanol, and propanol precursors. *Carbon*, 49:4204–4210, 2011.

[44] Z. Sun, Z. Yan, J. Yao, E. Beitler, Y. Zhu, and J. M. Tour. Growth of graphene from solid carbon sources. *Nature*, 468:549–552, 2010.

[45] W. Zhang, P. Wu, Z. Li, and J. Yang. First-Principles Thermodynamics of Graphene Growth on Cu Surfaces. *The Journal of Physical Chemistry C*, 115(36):17782–17787, 2011.

[46] S. Riikonen, A. V. Krasheninnikov, L. Halonen, and R. M. Nieminen. The Role of Stable and Mobile Carbon Adspecies in Copper-Promoted Graphene Growth. *The Journal of Physical Chemistry C*, 116(9):5802–5809, 2012.

[47] L. Gao, J. R. Guest, and N. P. Guisinger. Epitaxial Graphene on Cu(111). *Nano Letters*, 10(9):3512–3516, 2010.

[48] J. Gao, J. Yip, J. Zhao, B. I. Yakobson, and F. Ding. Graphene Nucleation on Transition Metal Surface: Structure Transformation and Role of the Metal Step Edge. *Journal of the American Chemical Society*, 133(13):5009–5015, 2011.

[49] H. Wang, G. Wang, P. Bao, S. Yang, W. Zhu, X. Xie, and W.-J. Zhang. Controllable Synthesis of Submillimeter Single-Crystal Monolayer Graphene Domains on Copper Foils by Suppressing Nucleation. *Journal of the American Chemical Society*, 134(8):3627–3630, 2012.

[50] L. Zhao, K. T. Rim, H. Zhou, R. He, T. F. Heinz, A. Pinczuk, G. W. Flynn, and A. N. Pasupathy. Influence of copper crystal surface on the CVD growth of large area monolayer graphene. *Solid State Communications*, 151(7):509 – 513, 2011.

[51] K. M. Reddy, A. D. Gledhill, C. Chen, J. M. Drexler, and N. P. Padture. High quality, transferrable graphene grown on single crystal cu(111) thin films on basal-plane sapphire. *Applied Physics Letters*, 98, 2011.

[52] Z. Yan, J. Lin, Z. Peng, Z. Sun, Y. Zhu, L. Li, C. Xiang, E. L. Samuel, C. Kittrell, and J. M. Tour. Toward the Synthesis of Wafer-Scale Single-Crystal Graphene on Copper Foils. *ACS Nano*, 6:9110–9117, 2012.

[53] D. L. Miller, M. W. Keller, J. M. Shaw, K. P. Rice, R. R. Keller, and K. M. Diederichsen. Giant secondary grain growth in Cu films on sapphire. *AIP Advances*, 3, 2013.

[54] A. M. Lewis, B. Derby, and I. A. Kinloch. Influence of Gas Phase Equilibria on the Chemical Vapor Deposition of Graphene. *ACS Nano*, 7(4):3104–3117, 2013.

[55] S. Bhaviripudi, X. Jia, M. S. Dresselhaus, and J. Kong. Role of kinetic factors in chemical vapor deposition synthesis of uniform large area graphene using copper catalyst. *Nano Letters*, 10(10):4128–4133, 2010.

[56] G. Ding, Y. Zhu, S. Wang, Q. Gong, L. Sun, T. Wu, X. Xie, and M. Jiang. Chemical vapor deposition of graphene on liquid metal catalysts. *Carbon*, 53:321–326, 2013.

[57] D. Geng, B. Wu, Y. Guo, L. Huang, Y. Xue, J. Chen, G. Yu, L. Jiang, W. Hu, and Y. Liu. Uniform hexagonal graphene flakes and films grown on liquid copper surface. *Proceedings of the National Academy of Sciences*, 109(21):7992–7996, 2012.

[58] T. Terasawa and K. Saiki. Growth of graphene on Cu by plasma enhanced chemical vapor deposition. *Carbon*, 50(3):869 – 874, 2012.

[59] I. Vlassiouk, M. Regmi, P. Fulvio, S. Dai, P. Datskos, G. Eres, and S. Smirnov. Role of Hydrogen in Chemical Vapor Deposition Growth of Large Single-Crystal Graphene. *ACS Nano*, 5(7):6069–6076, 2011.

[60] J. Ryu, Y. Kim, D. Won, N. Kim, J. S. Park, E. Lee, D. Cho, S. Cho, S. J. Kim, G. H. Ryu, H. Shin, Z. Lee, B. H. Hong, and S. Cho. Fast Synthesis of High-Performance Graphene Films by Hydrogen-Free Rapid Thermal Chemical Vapor Deposition. *ACS Nano*, 8(1):950–956, 2014.

[61] Y. Hao, M.S. Bharathi, L. Wang, Y. Liu, H. Chen, S. Nie, X. Wang, H. Chou, C. Tan, B. Fallahazad, H. Ramanarayan, C. W. Magnuson, E. Tutuc, B. I. Yakobson, K. F. McCarty, W. Zhang, P. Kim, J. Hone, L. Colombo, and R. S. Ruoff. The Role of Surface Oxygen in the Growth of Large Single-Crystal Graphene on Copper. *Science*, 342(6159):720–723, 2013.

[62] W. Wu, Q. Yu, P. Peng, Z. Liu, J. Bao, and S.-S. Pei. Control of thickness uniformity and grain size in graphene films for transparent conductive electrodes. *Nanotechnology*, 23(3):035603, 2012.

[63] Microchem, PMMA positive resists. `http://www.microchem.com/Prod-PMMA.htm`. Accessed: 9.7.2015.

[64] H. Seidel, L. Csepregi, A. Heuberger, and H. Baumgartel. Anisotropic Etching of Crystalline silicon in Alkaline Solutions, 1. Orientation Dependence and Behavior of Passivation Layers. *J. Electrochem. Soc.*, 137(11):3612–3626, 1990.

[65] A. Deraoui, K. Mallat, A. Cornet, and P. Defrance. Optical Properties of Micro and Nanostructured Bioinspired Materials. *International Journal of Optics and Applications*, 4(2):31–39, 2014.

[66] T. Mele, J. Nulman, and J. Krusius. Selective and anisotropic reactive ion etch of LPCVD silicon nitride with CHF3 based gases. *Journal of Vacuum Science & Technology B: Microelectronics and Nanometer Structures*, 2(4):684, October 1984.

[67] J. Song, F.-Y. Kam, R.-Q. Png, W.-L. Seah, J.-M. Zhuo, G.-K. Lim, P. K. H. Ho, and L.-L. Chua. A general method for transferring graphene onto soft surfaces. *Nature Nanotechnology*, 8:356–362, 2013.

[68] X. Liangi, B. A. Sperling, I. Calizo, G. Cheng, C. A. Hacker, Q. Zhang, Y. Obeng, K. Yan, H. Peng, Q. Li, X. Zhu, H. Yuan, A. R. Hight Walker, Z. Liu, L. Peng, and C. A. Richter. Toward Clean and Crackless Transfer of Graphene. *ACS Nano*, 5(11):9144–9153, 2011.

[69] C. Gong, H. C. Floresca, D. Hinojos, S. McDonnell, X. Qin, Y. Hao, S. Jandhyala, G. Mordi, J. Kim, L. Colombo, R. S. Ruoff, M. J. Kim, K. Cho, R. M. Wallace, and Y. J. Chabal. Rapid Selective Etching of PMMA Residues from Transferred Graphene by Carbon Dioxide. *The Journal of Physical Chemistry C*, 117(44):23000–23008, 2013.

[70] Y.-D. Lim, D.-Y. Lee, T.-Z. Shen, C.-H. Ra, J.-Y. Choi, and W. J. Yoo. Si-Compatible Cleaning Process for Graphene Using Low-Density Inductively Coupled Plasma. *ACS Nano*, 6(5):4410–4417, 2012.

[71] H. J. Jeong, H. Y. Kim, S. Y. Jeong, J. T. Han, K.-J. Baeg, J. Y. Hwang, and G.-W. Lee. Improved transfer of chemical-vapor-deposited graphene through modification of intermolecular interactions and solubility of poly(methylmethacrylate) layers. *Carbon*, 66:612 – 618, 2014.

[72] J. W. Suk, A. Kitt, C. W. Magnusson, Y. Hao, S. Ahmed, J. An, A. K. Swan, B. B. Goldberg, and R. S. Ruoff. Transfer of CVD-Grown Monolayer Graphene onto Arbitrary Substrates. *ACS Nano*, 5:6916–6924, 2011.

[73] Quorum Technologies. *E3000 Series Critical Point Drying Apparatus Operation Manual*. Document Number OM-E3000, Issue 3 (09/07).

[74] R. Egerton. *Physical Principles of Electron Microscopy: An Introduction to TEM, SEM, and AEM*. Springer Science & Business Media Inc., 1st edition, 2005.

[75] JEOL. Invitation to the SEM World. http://www.jeolusa.com/RESOURCES/ElectronOptics/DocumentsDownloads/tabid/320/Default.aspx?EntryId=257. Accessed: 10.7.2015.

[76] Transmission electron microscopy. http://en.wikipedia.org/wiki/Transmission_electron_microscopy. Accessed: 10.7.2015.

[77] Northern Arizona University. SEM Instrumentation. http://www4.nau.edu/microanalysis/microprobe-sem/instrumentation.html. Accessed: 10.7.2015.

[78] P. J. Larkin. *IR and Raman Spectroscopy: Principles and Spectral Interpretation*. Elsevier, 2011.

[79] Z. Ni, Y. Wang, T. Yu, and Z. Shen. Raman Spectroscopy and Imaging of Graphene. *Nano Research*, 1:273–291, 2008.

[80] A. C. Ferrari. Raman spectroscopy of graphene and graphite: Disorder, electron-phonon coupling, doping and nonadiabatic effects. *Solid State Communications*, 143:47–57, 2007.

[81] M. A. Pimenta, G. Dresselhaus, M. S. Dresselhaus, L. G. Cancado, A. Jorio, and R. Saito. Studying disorder in graphite-based systems by Raman spectroscopy. *Phys. Chem. Chem. Phys.*, 9:1276–1290, 2007.

[82] A. C. Ferrari, J. C. Meyer, V. Scardaci, C. Casiraghi, M. Lazzeri, F. Mauri, S. Piscanec, D. Jiang, K. S. Novoselov, S. Roth, and A. K. Geim. Raman Spectrum of Graphene and Graphene Layers. *Physical Review Letters*, 97:187401–1–187401–4, 2006.

[83] L. G. Cançado, A. Reina, J. Kong, and M. S. Dresselhaus. Geometrical approach for the study of G' band in the Raman spectrum of monolayer graphene, bilayer graphene, and bulk graphite. *Phys. Rev. B*, 77:245408, 2008.

[84] S. D. Costa, A. Righi, C. Fantini, Y. Hao, C. Magnuson, L. Colombo, R. S. Ruoff, and M. A. Pimenta. Resonant Raman spectroscopy of graphene grown on copper substrates. *Solid State Communications*, 152(15):1317–1320, 2012.

[85] V.-M. Hiltunen. Graphene synthesis by chemical vapor deposition and its characterization. Bachelor's thesis, University of Jyväskylä, 2014.

[86] X. Dong, P. Wang, W. Fang, C. Su, Y. Chen, L. Li, W. Huang, and P. Chen. Growth of large-sized graphene thin-films by liquid precursor-based chemical vapor deposition under atmospheric pressure. *Carbon*, 49:3672–3678, 2011.

[87] K. Celebi, M. T. Cole, K. B. K. Teo, and H. G. Park. Observations of Early Stage Graphene Growth on Copper. *Electrochemical and Solid-State Letters*, 15, 2012.

[88] B. Hu, H. Ago, C. M. Orofeo, Y. Ogawa, and M. Tsuji. On the nucleation of graphene by chemical vapor deposition. *New J. Chem.*, 36:73–77, 2012.

Appendices

Appendix 1: Additional images and spectra

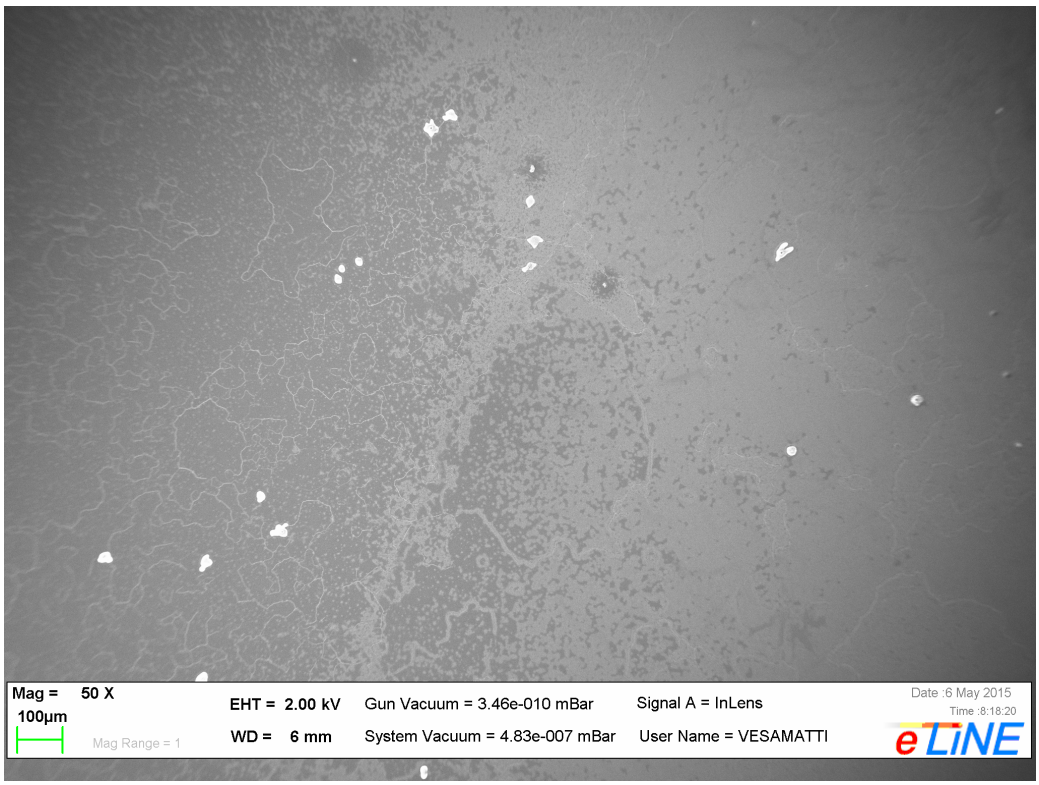

Figure A1: A low magnification SEM image of amorphous carbon-grahpene mix.

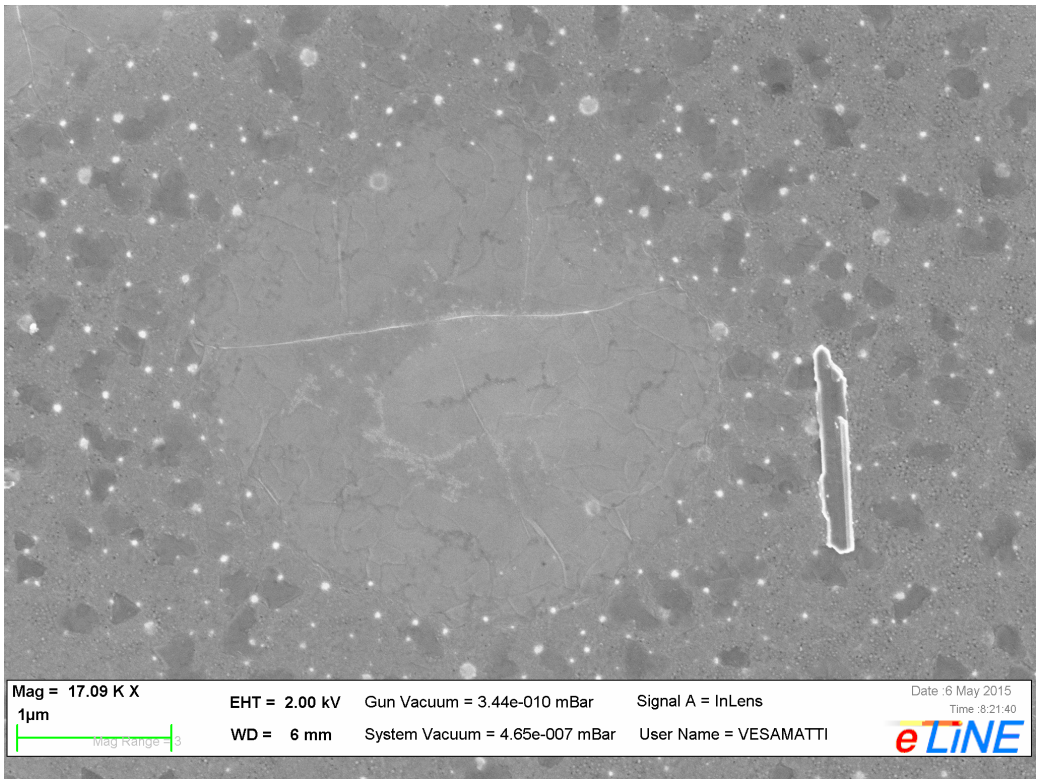

Figure A2: A high magnification SEM image of small graphene circle and amorphous carbon.

Figure A3: A high magnification SEM image of graphene on copper.

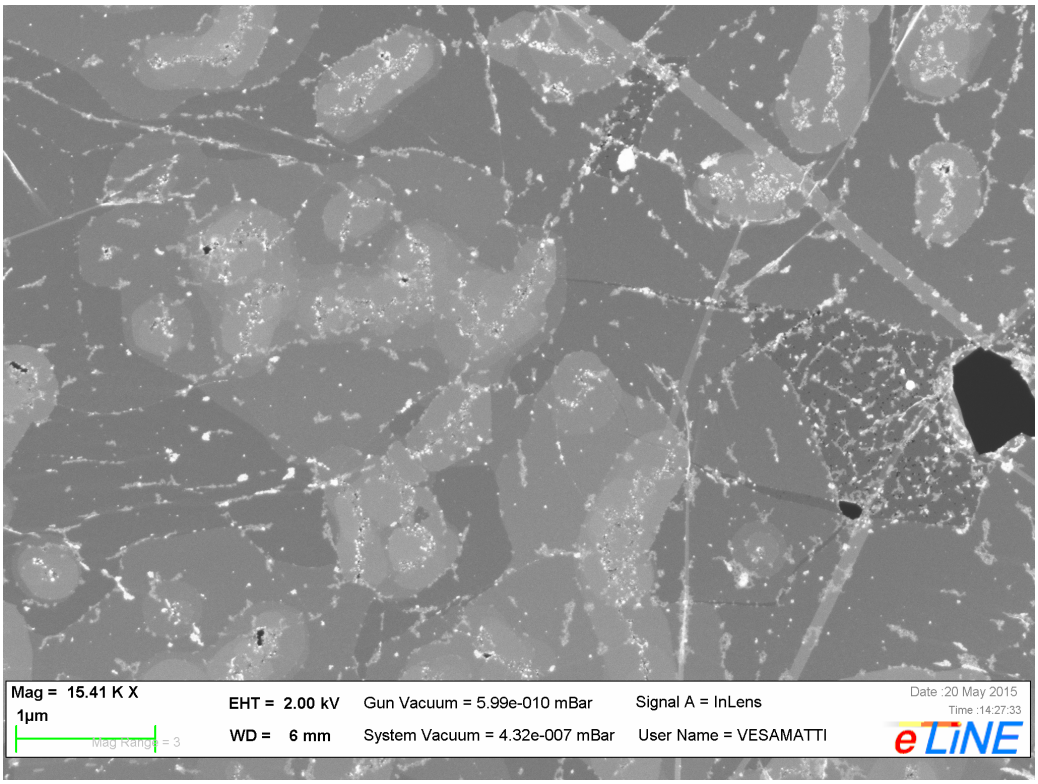

Figure A4: A high magnification SEM image of suspended graphene.

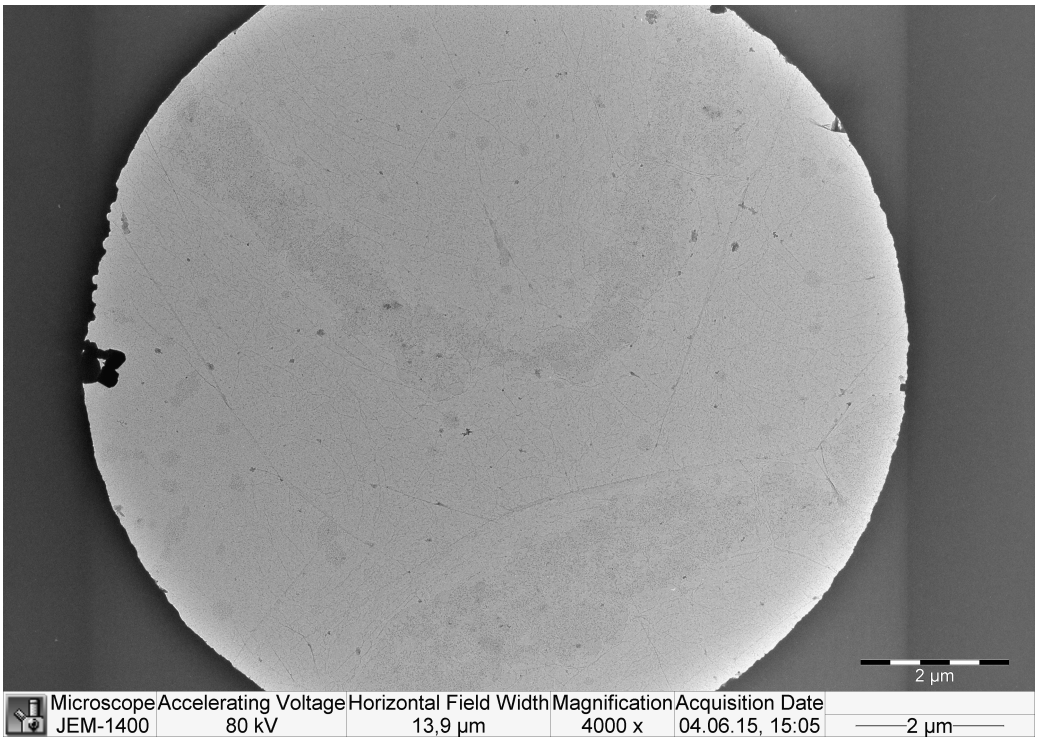

Figure A5: A TEM image of sample with multilayer graphene lines.

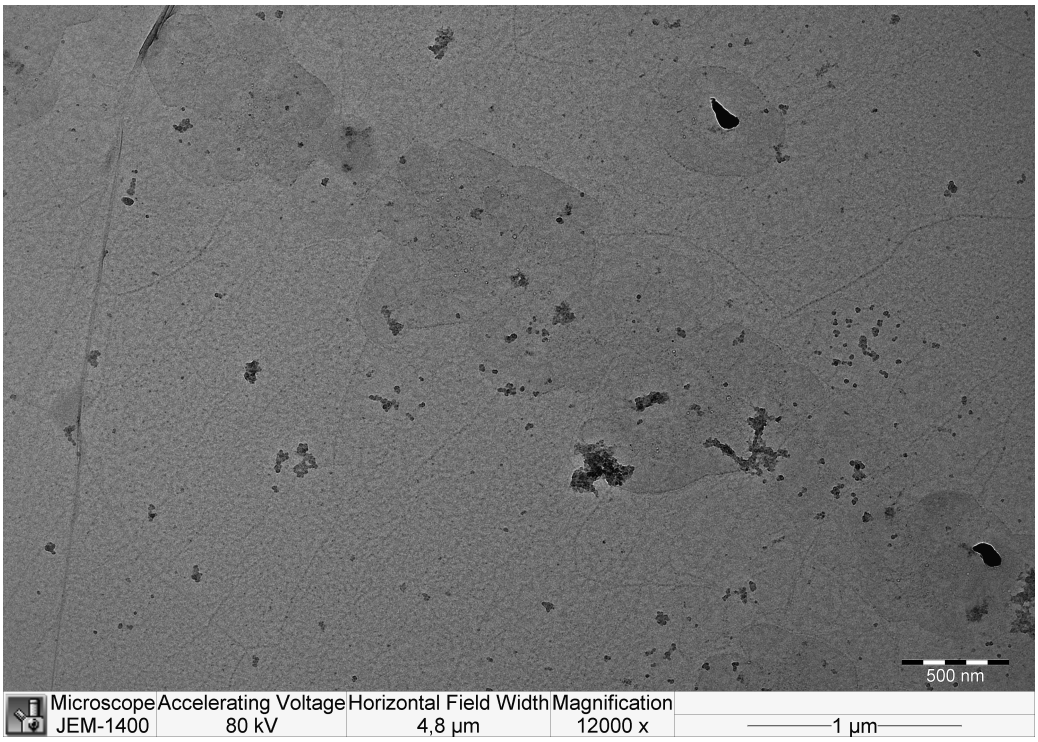

Figure A6: A high magnification TEM image of sample with multilayer graphene lines.

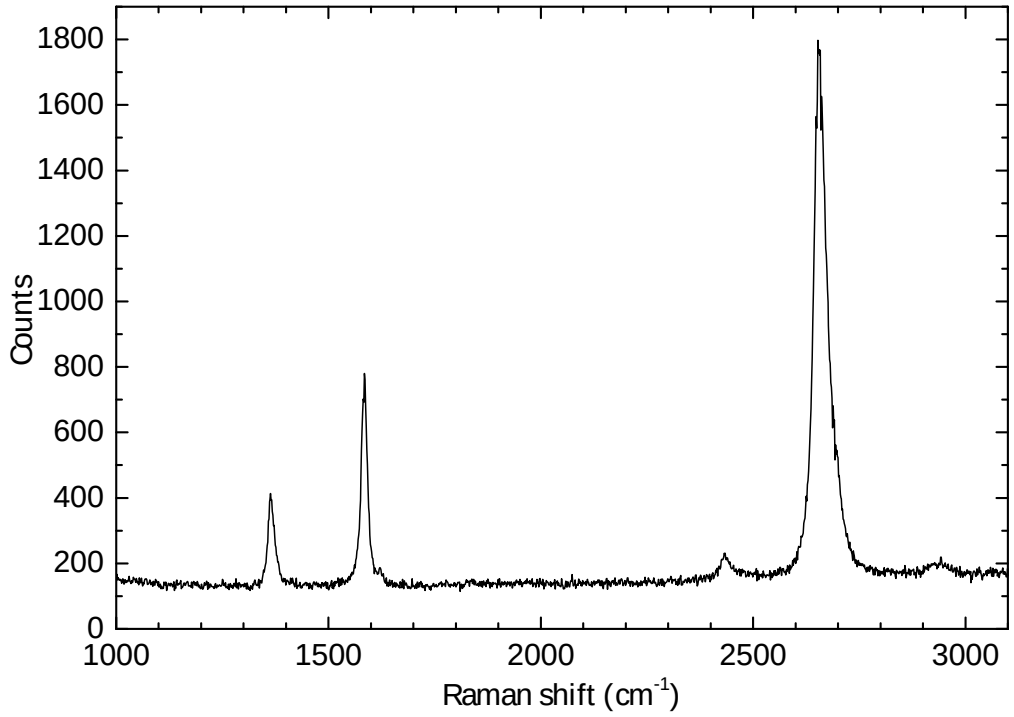

Figure A7: A Raman spectrum out of black areas in suspended graphene.

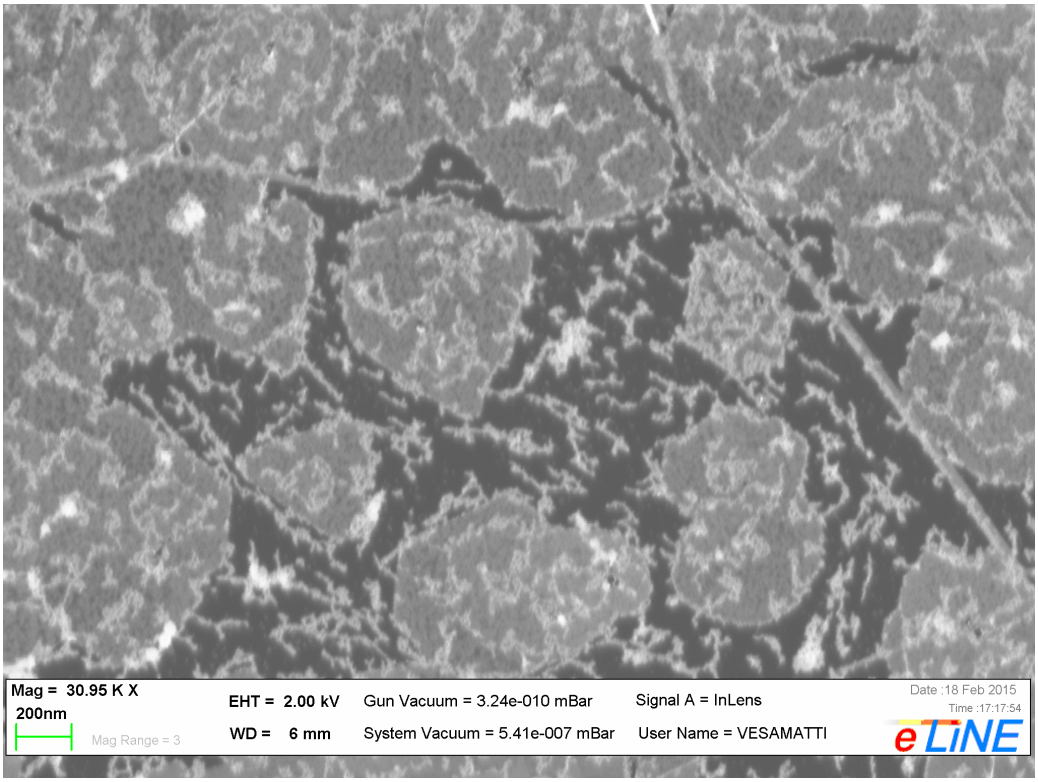

Figure A8: A SEM image with higher magnification.

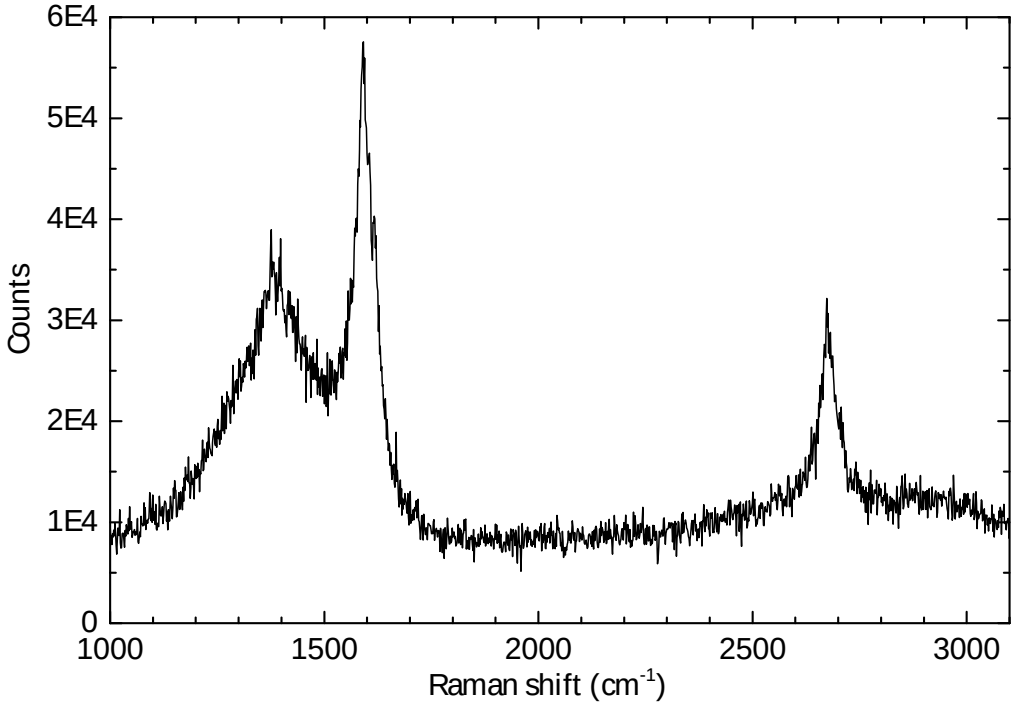

Figure A9: A Raman spectrum of suspended graphene sample in Figure 21a.

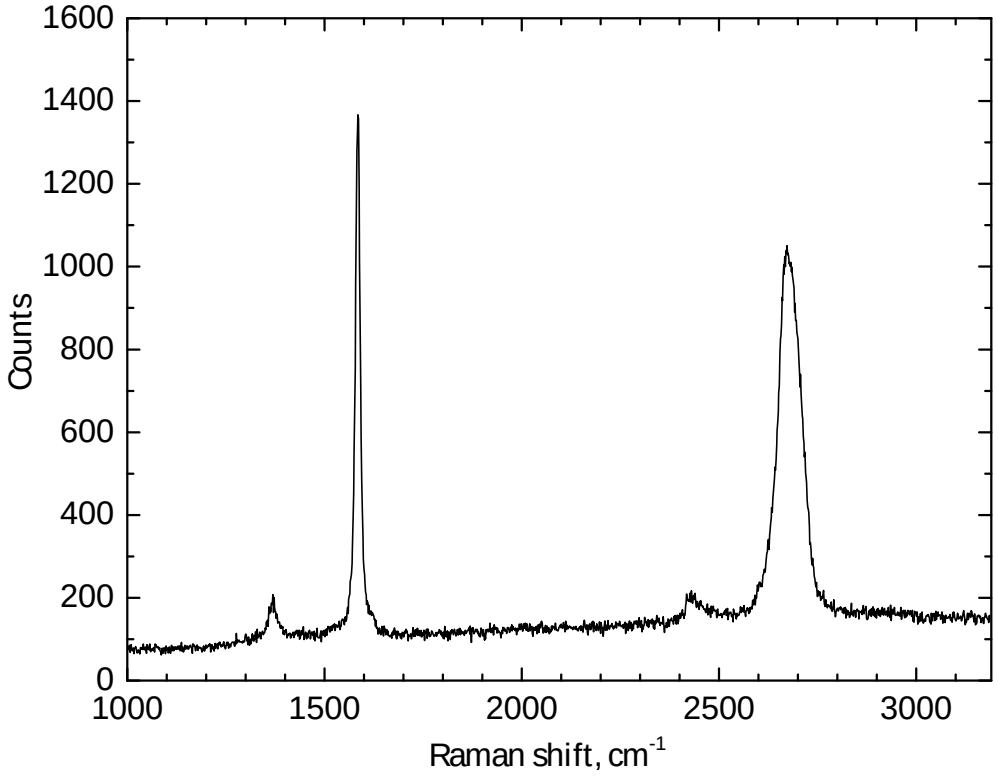

Figure A10: A Raman spectrum of suspended graphene sample in Figure 21b.

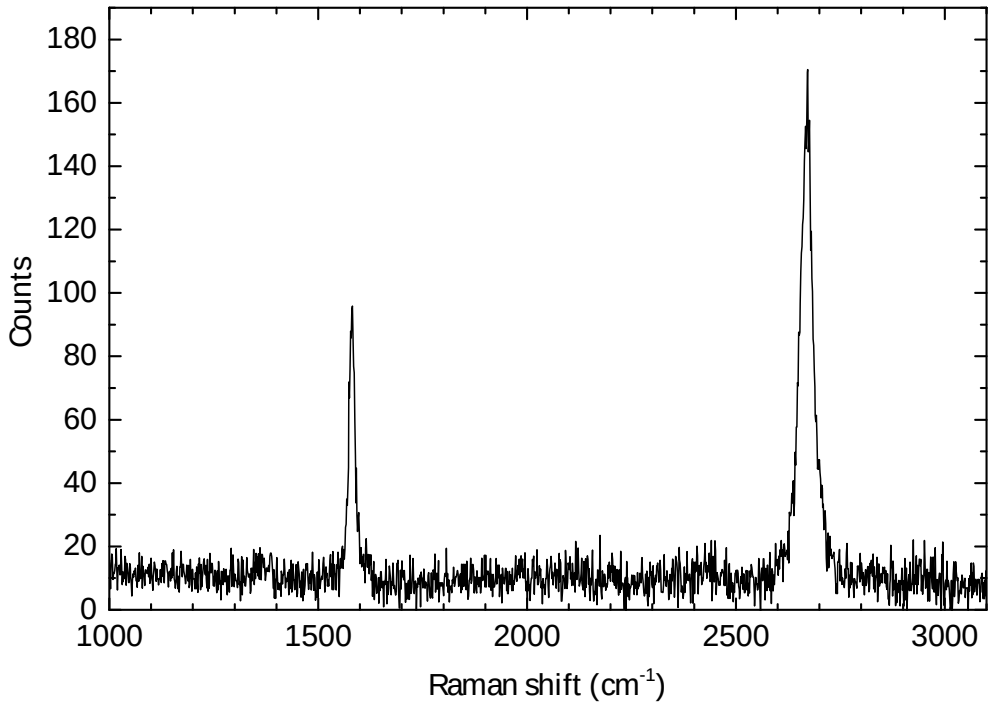

Figure A11: A Raman spectrum of suspended graphene sample in Figure 22a.

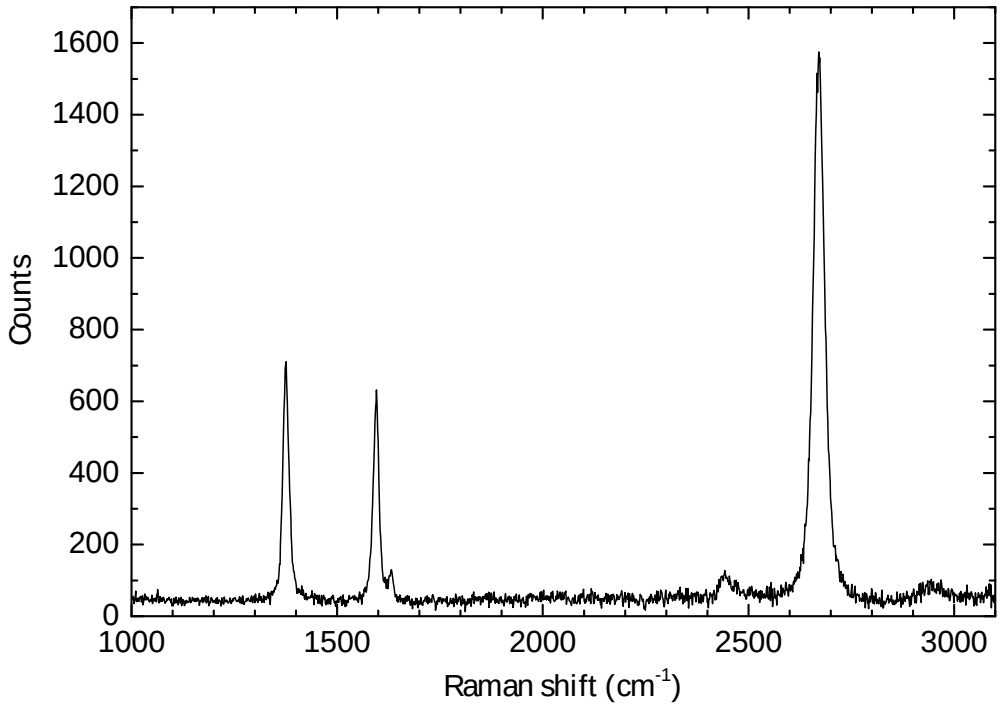

Figure A12: A Raman spectrum of suspended graphene sample in Figure 22b.

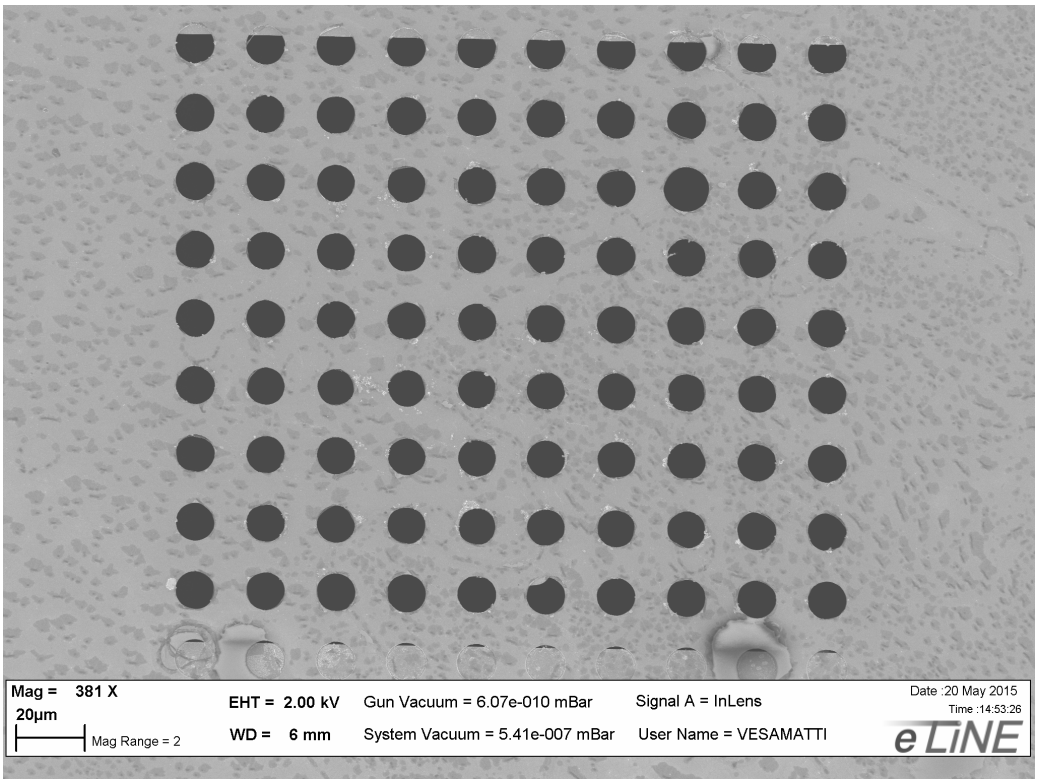

Figure A13: A SEM image of a monolayer graphene sample from which PMMA was removed by O_2 annealing.

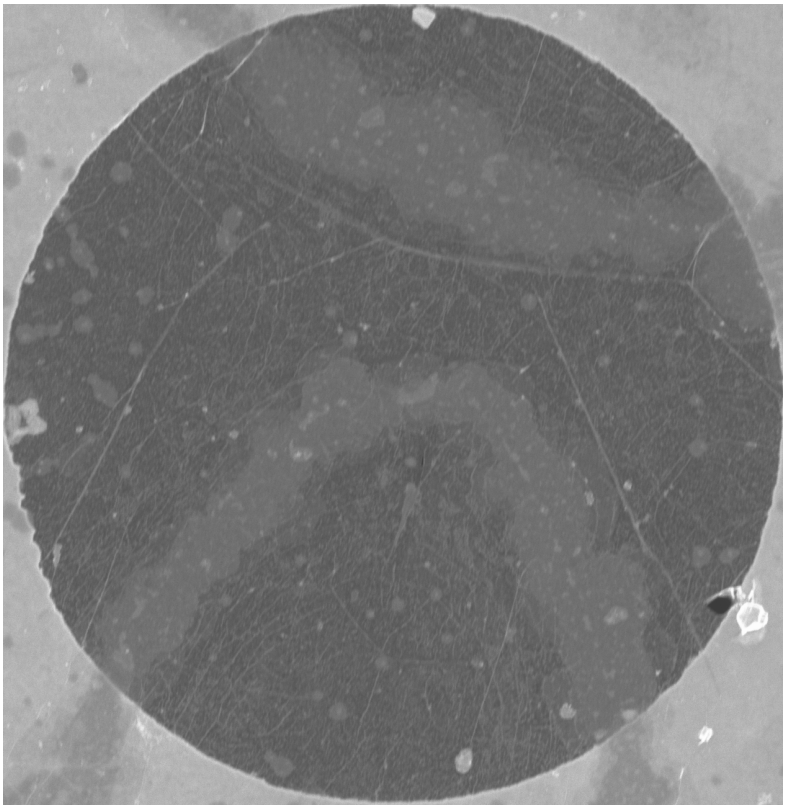

(a) Before

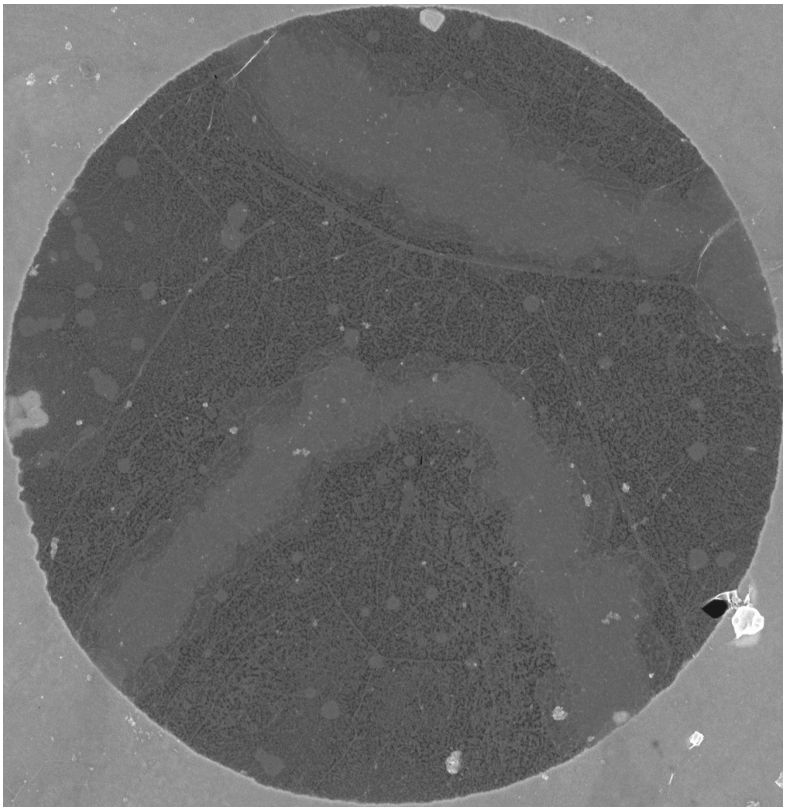

(b) After

Figure A14: Suspended graphene (a) before and (b) after O_2 annealing.

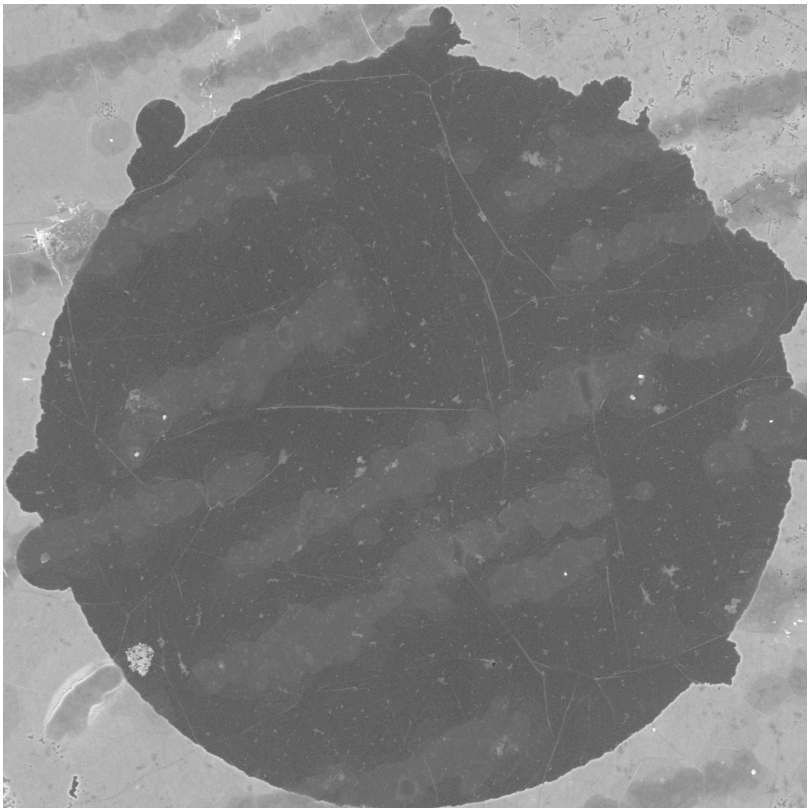

(a) Before

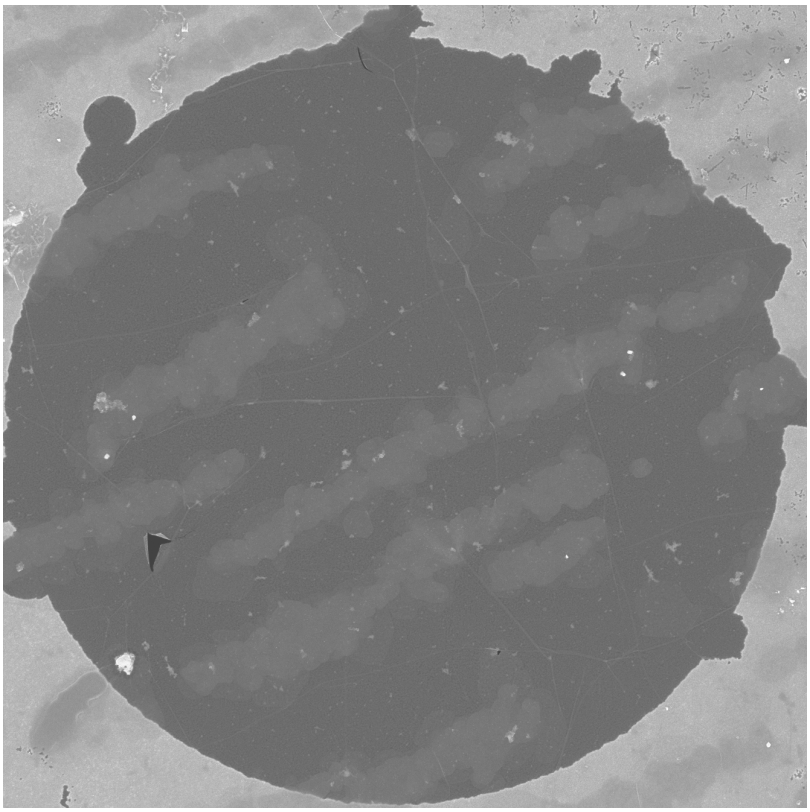

(b) After

Figure A15: Suspended graphene (a) before and (b) after N_2 annealing.